Solid Earth Discuss., 5, 963–1005, 2013
www.solid-earth-discuss.net/5/963/2013/
doi:10.5194/sed-5-963-2013

Solid Earth
Discussions
Open Access

Petrophysical constraints on the seismic properties of the Kaapvaal craton mantle root

V. Baptiste and A. Tommasi

Géosciences Montpellier, Université Montpellier 2 & CNRS, CC 60, Place E. Bataillon, 34095 Montpellier cedex 5, France

Received: 1 July 2013 – Accepted: 2 July 2013 – Published: 16 July 2013

Correspondence to: V. Baptiste (virginie.baptiste@gm.univ-montp2.fr)

Published by Copernicus Publications on behalf of the European Geosciences Union.

Abstract

We calculated the seismic properties of 47 mantle xenoliths from 9 kimberlitic pipes in the Kaapvaal craton based on their modal composition, the crystal preferred orientations (CPO) of olivine, ortho- and clinopyroxene, and garnet, the Fe content of olivine, and the pressures and temperatures at which the rocks were equilibrated. These data allow constraining the variation of seismic anisotropy and velocities with depth. The fastest P wave and fast split shear wave (S1) polarization direction is always close to olivine [100] maximum. Changes in olivine CPO symmetry result in minor variations in the seismic anisotropy patterns. Seismic anisotropy is higher for high olivine contents and stronger CPO. Maximum P waves azimuthal anisotropy (AV_p) ranges between 2.5 and 10.2 % and S waves polarization anisotropy (AV_s) between 2.7 and 8 %. Seismic properties averaged in 20 km thick intervals depth are, however, very homogeneous. Based on these data, we predict the anisotropy that would be measured by SKS, Rayleigh (S_V) and Love (S_H) waves for 5 end-member orientations of the foliation and lineation. Comparison to seismic anisotropy data in the Kaapvaal shows that the coherent fast directions, but low delay times imaged by SKS studies and the low azimuthal anisotropy and S_H faster than S_V measured using surface waves may only be consistently explained by dipping foliations and lineations. The strong compositional heterogeneity of the Kaapvaal peridotite xenoliths results in up to 3 % variation in density and in up to 2.3 % of variation V_p, V_s and the V_p/V_s ratio. Fe depletion by melt extraction increases V_p and V_s, but decreases the V_p/V_s ratio and density. Orthopyroxene enrichment decreases the density and V_p, but increases V_s, strongly reducing the V_p/V_s ratio. Garnet enrichment increases the density, and in a lesser manner V_p and the V_p/V_s ratio, but it has little to no effect on V_s. These compositionally-induced variations are slightly higher than the velocity perturbations imaged by body-wave tomography, but cannot explain the strong velocity anomalies reported by surface wave studies. Comparison of density and seismic velocity profiles calculated using the xenoliths' compositions and equilibrium conditions to seismological data in the Kaapvaal

SED
5, 963–1005, 2013

highlights that: (i) the thickness of the craton is underestimated in some seismic studies and reaches at least 180 km, (ii) the deep sheared peridotites represent very local modifications caused and oversampled by kimberlites, and (iii) seismological models probably underestimate the compositional heterogeneity in the Kaapvaal mantle root, which occurs at a scale much smaller than the one that may be sampled seismologically.

1 Introduction

A wealth of seismological studies have investigated the structure of the Kaapvaal craton, aiming at unraveling the thermal structure, the composition, and the deformation fabric of the cratonic root and at understanding the causes of its stability since Archean times, as inferred from Re–Os model ages obtained in kimberlite-born mantle xenoliths (Pearson et al., 1995). Tomographic models and receiver function data agree on the presence of a high velocity upper mantle lid on top of a low velocity layer (Jordan, 1978; Priestley, 1999; James et al., 2001; Li and Burke, 2006; Priestley et al., 2006). Most body and surface waves tomography models indicate that this lid is 200–250 km thick beneath the Kaapvaal craton (James et al., 2001; Chevrot and Zhao, 2007; Fishwick, 2010). A slightly thinner high velocity layer, between 150 and 180 km, was, however, imaged by other models (Sebai et al., 2006; Wang et al., 2008). Recent receiver function studies suggest, on the other hand, the presence of a ∼100 km thick low velocity zone below a 150–200 km root (Hansen et al., 2009; Adams and Nyblade, 2011).

Discriminating between these models, which point to different cratonic root thicknesses, and interpreting these geophysical data in terms of composition and temperature requires independent observations. The high seismic velocities beneath the Kaapvaal craton have been alternatively attributed to thermal effects (Priestley and Tilmann, 2009) or to changes in composition (Begg et al., 2009). Smaller scale variations in seismic properties within the cratonic root cannot also be neither imaged nor interpreted unambiguously. Beneath the Bushveld complex, some but not all body-wave to-

SED
5, 963–1005, 2013

mography models imaged lower velocities than the average ones in the craton, which have been attributed to either more fertile compositions associated with the 2 Ga-old Bushweld magmatism (James et al., 2001; Fouch et al., 2004a), or to a hotter present-day geotherm (Fouch et al., 2004a). Receiver functions also image intra-lithosphere reflectors suggesting a vertical stratification of the composition, due to metasomatic infiltration of melts, or anisotropy contrasts within the cratonic root (Wittlinger and Farra, 2007; Savage and Silver, 2008).

The deformation of the Kaapvaal craton has been investigated by seismic anisotropy studies (Silver et al., 2001, 2004; Fouch et al., 2004a,b; Adam and Lebedev, 2012; Vinnik et al., 1995, 2012). Silver et al. (2001) measured small SKS delay times of 0.62 s on average with almost null delays in the central Kaapvaal craton. They observed consistent fast polarization directions following the trend of geological structures, which they attributed to anisotropy in the lithosphere. Vinnik et al. (1995) attributed the same NNE-SSW fast polarization directions to asthenospheric deformation in response to African plate motion. Significant variations of SKS delay times were measured near Kimberley, which was interpreted as the boundary between a strongly anisotropic and a weakly anisotropic domain (Fouch et al., 2004b). More recently, a Rayleigh wave azimuthal anisotropy model (Adam and Lebedev, 2012) proposed that the mantle fabric at lithospheric depths parallels the Archean–Paleoproterozoic crustal structures in the Limpopo belt and in the northern Kaapvaal, but is perpendicular to the crustal structures in the western part of the craton. Vinnik et al. (2012), using *P* receiver functions and SKS waveforms inversion, observed similar fast directions in the uppermost mantle near the Limpopo belt. They also detected a change with depth in the orientation of the fast direction from 70° to ∼ 40°, which aligns progressively with current plate motion at depths > 160 km. In conclusion, seismic anisotropy data obtained using different waves is mostly, but not always consistent and their interpretation is not unique, needing to be constrained by direct observations of the lithospheric mantle deformation and resulting anisotropy.

SED
5, 963–1005, 2013

The Kaapvaal craton was affected by numerous kimberlite eruptions, mostly between the Late Jurassic and the Cretaceous, but also during the Meso–Proterozoic and Paleozoic (Kramers and Smith, 1983; Allsopp et al., 1985; Phillips et al., 1998). These lavas carried xenoliths, which provide direct sampling of the lithospheric mantle beneath the craton. Seismic properties of these peridotite xenoliths can be calculated from their crystal-preferred orientation and composition data (Mainprice and Silver, 1993; Mainprice and Humbert, 1994). Such data constrain the possible seismic velocities and anisotropies within the Kaapvaal mantle root, as well as their dependence on the peridotites composition and crystals preferred orientations. In the present study, we calculated the anisotropic seismic properties of 47 peridotite xenoliths from 9 kimberlite pipes, which sample different domains and depths in the Kaapvaal mantle root (Fig. 1). The present study represents a significant enrichment of the database of seismic properties of the Kaapvaal mantle root, as previous studies focused on either the composition- and depth-dependence of the isotropic seismic velocities (James et al., 2004) or the crystal preferred orientation-induced anisotropy (Ben Ismail et al., 2001).

2 The studied data set

The 47 peridotite xenoliths used in this study come from 9 kimberlitic pipes (Kimberley, Jagersfontein, Monastery, Lentseng, De Beers, Finsch, Kamfersdam, Premier, and Mothae) from the Kaapvaal craton, with ages ranging from 1200 to 87 Ma. These peridotites are mainly composed of olivine, orthopyroxene, clinopyroxene ± garnet. When spinel is present, it is a minor phase.Thermobarometry data indicates that they were equilibrated at depths ranging between 83 and 187 km (Baptiste et al., 2012). The full description of the microstructures, crystal-preferred orientations (CPOs), and data on the water contents in olivine and pyroxenes in these xenoliths is presented in Baptiste et al. (2012), but their main characteristics are recalled below. The modal content, texture, olivine CPO-type and intensity, and equilibrium P-T conditions of all studied samples are summarized in Table 1.

SED
5, 963–1005, 2013

The studied mantle xenoliths can be separated into two textural groups: the coarse-grained and the sheared peridotites. The coarse-grained peridotites are the dominant textural group (72 % of the studied samples), being observed at all depths and in all pipes (Fig. 1). They display most often strongly annealed textures, but coarse-porphyroclastic microstructures are also common. The sheared peridotites are only observed in the deeper part of the sampled columns (equilibrium pressures > 4.5 GPa). Their textures range from mylonitic to fluidal or mosaic-like, probably due to variable post-deformational annealing. Based on their occurrence, microstructures and thermal evolution, Baptiste et al. (2012) interpreted the coarse-grained microstructures as the typical cratonic root microstructure, resulting from an early deformation episode followed by a long quiescence time, and the sheared peridotites as recording local modifications of the cratonic microstructure, just before the xenoliths extraction. Their formation is probably associated with the kimberlitic activity as proposed by Green and Guegen (1974).

Coarse-grained peridotites have in average more refractory compositions than the sheared peridotites.They are mainly harzburgites, with high orthopyroxene contents (> 20 %). Sheared peridotites are mainly lherzolites, with highly variable garnet contents (0–18 %). In the studied samples, olivine water contents are very variable; maximum water contents increase up to 150 km depth, reaching up to 150 wt. ppm H_2O (values obtained using the Bell et al. (2003) calibration; Baptiste et al., 2012). In contrast, olivines from samples equilibrated at depths > 150 km are almost dry.

3 Methods

Seismic properties of Kaapvaal xenoliths were calculated based on the olivine, orthopyroxene, clinopyroxene, and garnet CPOs, and on modal compositions estimated from electron-backscattered diffraction (EBSD)-based crystal orientation maps, which covered the entire thin section (Mainprice, 1990). Because olivine is the dominant phase in these peridotites and largely determines their seismic properties, olivine elastic ten-

SED
5, 963–1005, 2013

sors were recalculated to account for the actual olivine Mg# in each sample, based on the single-crystal elastic constant tensors for fayalite, forsterite, and olivine with Mg# of 90, 91 and 93 (Kumazawa and Anderson, 1969; Suzuki et al., 1983; Webb et al., 1989; Isaak et al., 1993; Abramson et al., 1997). For orthopyroxene, clinopyroxene, and garnet, the single crystal elastic tensors of Chai et al. (1997a), Collins and Brown (1998), and Chai et al. (1997b) at ambient pressure (P) and temperature (T) were used. To account for the effect of pressure and temperature on the seismic properties, elastic tensors and density of olivine, pyroxenes, and garnet were recalculated every 10 km for depths between 40 and 200 km using the AnisPT8 software by D. Mainprice, based on published pressure and temperature derivatives of the elastic constants (Abramson et al., 1997; Chai et al., 1997a,b; Collins and Brown, 1998) and the Kaapvaal geotherm of Baptiste et al. (2012).

The elastic constants and resulting seismic properties of each sample were calculated both at ambient pressure and temperature conditions and at its equilibrium pressure and temperature. A Voigt–Reuss–Hill averaging was applied in all calculations. Calculated seismic properties and elastic constants of all samples are summarized in Tables 1 and 2, respectively. The three-dimensional distribution of seismic velocities and birefringence of S waves relatively to the samples' structural reference frame are displayed on lower hemisphere stereograms.

The mean seismic properties of six 20 km-deep sections between 70 and 190 km depth were calculated by averaging the olivine composition and modal contents and adding up the crystal preferred orientations of all samples equilibrated within the corresponding depth interval. This approach results in an upper bound for the estimated anisotropy, since the CPO summation is performed considering that all samples have a similar structural reference frame, that is, that the orientation of the foliation and lineation remains coherent within each depth interval.

To analyze the relations between the olivine CPO symmetry and intensity and the seismic anisotropy, the olivine CPO symmetry was characterized using the dimension-

SED
5, 963–1005, 2013

less BAindex defined as:

$$BA_{index} = \frac{1}{2}\left(2 - \left(\frac{P_{010}}{G_{010} + P_{010}}\right) - \left(\frac{G_{100}}{G_{100} + P_{100}}\right)\right) \quad (1)$$

This index allows the classification of the olivine CPO into 3 types: axial [010] (BA < 0.4), orthorhombic (0.4 < BA < 0.6), and axial [100] (BA > 0.6). The BA index was calculated using the MTEX texture analysis toolbox (Hielscher and Schaeben, 2008; Mainprice et al., 2011).

The olivine CPO intensity is characterized by the dimensionless J index, which is the volume-averaged integral of the squared orientation densities defined as:

$$J = f(g)^2 \, \mathrm{d}g \quad (2)$$

where $f(g)$ is the orientation distribution function (ODF) and $\mathrm{d}g = \mathrm{d}\varphi_1 \mathrm{d}\varphi \mathrm{d}\varphi_2 \sin\varphi\pi^2$. φ_1, φ, and φ_2 are the euler angles that define the rotations allowing for coincidence between the crystallographic and external reference frames. In natural peridotites, olivine CPO J indexes varies between 2 and 20, with a peak at 8–10 (Ben Ismaïl and Mainprice, 1998; Tommasi et al., 2000). J indexes were calculated based on the mean orientation of each grain, using the SuperJctf program by D. Mainprice (ftp://www.gm.univ-montp2.fr/mainprice//CareWare_Unicef_Programs/) with a 10° Gaussian half-width, 1° cells, and truncation of the orientation distribution function (ODF) at degree 22.

4 Results

4.1 Seismic anisotropy

Seismic anisotropy patterns for samples representative of the different microstructures and olivine CPO symmetry patterns observed among Kaapvaal xenoliths (Table 1 and Baptiste et al., 2012) are illustrated in Fig. 2. At first order, seismic anisotropy patterns

SED
5, 963–1005, 2013

for all samples have similar characteristics, independently of the peridotite microstructure and olivine CPO symmetry. The fastest and slowest P wave and slow S wave (S_2) propagation directions are aligned with the olivine [100] and [010] axes maxima, respectively.This orientation of the [100] maximum also controls the direction of polarization of the fast S waves.Moreover, when the lineation and foliation could be identified, this [100] maximum corresponds to the lineation. The fast split shear wave (S_1) is thus polarized in a plane containing the propagation direction and the lineation. The highest V_p/V_{s_1} ratio is always parallel to the lineation, when the lowest V_p/V_{s_1} ratio is located in the YZ plane.

Changes in olivine CPO symmetry result in second order variations in the seismic anisotropy patterns. Peridotites displaying an axial [100] CPO tend to show slow P waves velocities for all directions normal to the lineation, instead of a clear V_p minimum at high angle to the foliation.S waves polarization anisotropy patterns are also sensitive to the CPO symmetry. Samples with an axial [100] olivine CPO display high V_s anisotropy (AV_s) for directions of propagation in the foliation plane, but at high angle to the lineation (Y structural direction) and a minimum anisotropy for propagation along the lineation (X direction) and more rarely at 45° to the lineation in the XZ plane. The slowest S_1 waves propagation is always located at high angle to the foliation (Z structural direction), while the fastest is in the foliation plane, at 45° to the lineation. S_2 waves velocity is maximum close to the lineation or in the XZ plane, at ~ 10° to the lineation. The highest V_p/V_{s_2} ratio is always parallel to the lineation, while the lowest V_p/V_{s_2} ratio is minimum at high angle to the foliation (Z structural direction).

In contrast, peridotites with an axial [010] CPO show high S waves polarization anisotropy for propagations along the foliation plane and low anisotropy for S waves travelling at high angle to the foliation. More rarely, the highest S waves polarization anisotropy is observed close to the Y structural direction, whereas the minimum polarization anisotropy is at 45° to the lineation. S_1 waves velocity patterns are more variable.S_1 waves velocity is high along the entire foliation plane. The fastest S_1 waves may be, however, either aligned with both X and Y structural directions or at 45° to

SED
5, 963–1005, 2013

the lineation.S_2 waves velocity is always maximum close to the lineation and minimum along the YZ plane. The V_p/V_{s_2} ratio tends to show high values in the foliation plane, while the lower values are found at high angle to foliation (Z structural direction).

Peridotites with an orthorhombic CPO show patterns intermediate between the two previously described. Several samples exhibit a S wave polarization anisotropy pattern similar to that observed for samples with an axial [100] CPO. In other cases, maximum S waves polarization anisotropy is observed between to the Y structural direction and the lineation, while the minimum anisotropy is at high angle to the foliation. The S_1 waves velocity is most of time the highest along the foliation plane, parallel to both X and Y structural directions, or at 45° to these axes. The slowest S_1 waves propagation is located at high angle to the foliation (Z structural direction). The S_2 waves velocity is maximum parallel to the lineation, or 45° to the lineation, in the XZ plane. It is minimum along the YZ plane, sometimes more specifically parallel to both Y and Z structural directions. The maximum V_p/V_{s_2} ratio is observed along the foliation plane, and the minimum ration is located close to the Z structural direction.

Peridotites with a bimodal olivine CPO have also intermediate patterns, with maximum S wave polarization anisotropy for propagation directions close to the Y structural direction; minimum anisotropy is observed for propagation directions at 45° to the lineation in the XZ plane. In few other cases, S waves polarization anisotropy is minimum at high angle to the foliation. S_1 waves velocity is the highest in the foliation plane, close to both X and Y structural directions, while it is the lowest at high angle to the foliation (Z structural direction). The maximum S_2 waves velocity is maximum along the YZ plane. The V_p/V_{s_2} ratio is maximum along the foliation and minimum at high angle to the foliation (Z structural direction).

Despite the weak variation in the patterns, xenoliths from the Kaapvaal craton show a wide range of seismic anisotropy intensities (Fig. 3 and Table 1). Maximum anisotropy values range between 2.5 and 10.2 % for P waves azimuthal anisotropy (AV_p), between 2.7 and 8 % for S waves polarization anisotropy (AV_s), between 0.8 and 6.1 % for S_1 waves propagation anisotropy (AV_{S_1}), and between 0.5 and 6.4 % for

SED
5, 963–1005, 2013

S_2 waves propagation anisotropy (AV_{S_2}). All anisotropies show a positive covariance with the olivine CPO strength (Fig. 3a, b); samples with stronger olivine CPOs are more anisotropic.Yet, in agreement with previous studies (Ben Ismail and Mainprice, 1998), this variation is not linear: peridotites with J index > 4 tend to display a weak variation of the maximum anisotropy values. Coarse-grained peridotites show more variable olivine CPO intensities (J indexes range between 2–11), but their maximum seismic anisotropies are in the same range as those displayed by the sheared peridotites (Fig. 3a, b). This suggests that the modal composition has also an important effect on the seismic anisotropy of these samples.

The presence of pyroxenes and garnet is known to dilute the bulk anisotropy of the rock (Mainprice and Silver, 1993; Mainprice et al., 2000). Samples with high modal olivine, and therefore lower pyroxene and/or garnet contents, tend to have higher maximum AV_p, AV_{S_1} and AV_{S_2}. However, the dependence is weaker than the one on the olivine CPO strength (compare Fig. 3c,a). The dependence on the olivine content is even less marked for the S wave polarization anisotropy (Fig. 3d).

There is no simple relation between the olivine CPO symmetry, characterized by the BA index, and the maximum P-, S-, S_1-, and S_2 waves anisotropy (Fig. 3e, f). Samples with an olivine axial-[100] CPO tend to show higher maximum P and S_2 propagation anisotropies than those with an orthorhombic CPO, which are themselves more anisotropic than those with an axial-[010] CPO. The relation is less clear, however, for S wave polarization and S_1 propagation anisotropies.Moreover, this relation probably reflects more a variation in the olivine CPO intensity then a strong dependence on the olivine CPO symmetry. In the studied dataset, samples with axial-[100] tend to have stronger olivine CPO, but this behavior is not a general one in naturally deformed peridotites, which may also display very strong axial-[010] olivine CPO patterns (e.g., Tommasi et al., 2008).

SED
5, 963–1005, 2013

4.2 Effect of compositional variations on the density and isotropic seismic velocities

Kaapvaal mantle xenoliths record a long and complex history. Early partial melting and extraction of high melt fractions are evidenced by the depleted compositions (olivine Mg# > 92), which are common among the coarse-grained peridotites.However, the large variability in modal and chemical compositions of these xenoliths implies that the craton mantle root has been subsequently modified by multiple metasomatic events.The high orthopyroxene content observed in many coarse-grained peridotites has been attributed to percolation of Si-rich fluids and/or melts (e.g., Bell et al., 2005; Wasch et al., 2009; Baptiste et al., 2012). In many xenoliths, secondary crystallization of phlogopite, clinopyroxene and garnet points to reactions with percolating K-rich melts at high pressure (e.g., Grégoire et al., 2003; Griffin et al., 2003; Bell et al., 2005; Baptiste et al., 2012).These metasomatic events may have also allowed for re-hydration of the central part of the Kaapvaal mantle root (Baptiste et al., 2012). Finally, local high-stress deformation, which was probably associated with a late metasomatic event by K-rich fluids and/or melt (Wasch et al., 2009), produced the sheared peridotites (Baptiste et al., 2012).

This compositional variability resulted in significant variations in both density and seismic velocities as illustrated in Fig. 4, where densities and isotropic *P* and *S* wave velocities at ambient conditions are displayed as a function of the olivine Mg#, the orthopyroxene and the garnet content of each sample. The density of Kaapvaal samples varies by up to 3 % (Fig. 4a, e, i). It decreases with increasing olivine Mg# and orthopyroxene content, but strongly increases with increasing garnet content. The linear correlation with the garnet content is particularly striking. This later effect is dominant in the sheared peridotites, where the garnet content may attain up to 15 %.

P wave velocities vary by up to 2.2 % with the peridotites composition (Fig. 4b, f, j). There is a weak positive covariance between *P* waves velocities and garnet content. *P* wave velocities in coarse-grained peridotites also tend to increase with increasing

SED
5, 963–1005, 2013

olivine Mg# (Fig. 4b) and decreasing orthopyroxene content (Fig. 4f), but the competing effects of olivine Mg# and orthopyroxene content result in dispersion of P wave velocities of the coarse-grained peridotites in all diagrams. In contrast, P wave velocities in sheared peridotites increase strongly with olivine Mg#, probably because the latter have lower orthopyroxene contents.

The isotropic S wave velocities of the Kaapvaal mantle xenoliths show a clear linear correlation with olivine Mg# (Fig. 4c), varying by up to 2.4 %. This variation is consistent with previous data showing that an increase in the olivine Mg# from 88 to 94 in a dunite results in a linear increase in V_s by 1.5 % (Tommasi et al., 2004). No clear co-variation is observed between the orthopyroxene and garnet contents and V_s in neither coarse-grained nor sheared peridotites, although S-wave velocities are in average higher in the coarse-grained peridotites that also have higher orthopyroxene contents (Fig. 4g, k).

The V_p/V_s ratio is also sensitive to compositional changes (Fig. 4d, h, l), varying by up to 2.3 %. It decreases with increasing olivine Mg# and orthopyroxene content and increases with garnet content. The V_p/V_s ratio is very sensitive to orthopyroxene content, as indicated by the strong linear correlation between the two parameters (Fig. 4h). Sheared peridotites have higher and less variable V_p/V_s ratio than coarse-grained peridotites, probably due to their lower modal orthopyroxene.

4.3 Evolution of seismic properties and density with depth

The variation of the isotropic P and S wave velocities (V_p, V_s), V_p/V_s ratio, and density with depth in the present Kaapvaal xenolith suite and in the one studied by James et al. (2004) are plotted on Fig. 5. The isotropic P waves velocities calculated for the actual equilibrium depth and composition of our samples do not show a monotonic increase with increasing depth.They are highly heterogeneous, being comprised between 8.17 and 8.36 km s^{-1} over the whole column. This result contrasts with the one from James et al. (2004), who observed an increase in V_p up to 180 km depth and a brutal decrease below this depth. One may argue that the present data set does not sample well the deepest part of the root (below 180 km), but at all depths the peridotites

SED
5, 963–1005, 2013

analyzed in this study tend to display higher P wave velocities than those reported by James et al. (2004). In contrast, the isotropic S waves velocities decrease and the V_p/V_s ratio increase almost linearly with depth, in excellent agreement with the results of James et al. (2004). Density increases with depth, but the dispersion is higher than for V_s or the V_p/V_s ratio, probably due to the stronger dependence on the composition.

Compositions, olivine CPOs and anisotropic seismic properties of average samples (obtained by summing the CPO and averaging the compositions of all samples in a 20 km thick depth interval) for six depths between 70 and 190 km depth are presented in Fig. 6. With increasing depth, olivine and garnet contents increase, while the orthopyroxene content decreases. The variability of olivine Mg# increases as well, with a higher proportion of normal to Fe-rich olivines in the deeper part of the cratonic root, and the olivine CPO patterns change from axial-[100] to more orthorhombic.These variations do not result, however, in marked changes in seismic anisotropy with depth.

The maximum P waves anisotropy varies between 4.5 and 7.9 %. The fastest P waves propagation direction is always aligned with the olivine [100] axes maximum, that is, with the lineation. Between 70 and 110 km, P wave propagation is slow in all directions at high angle to the olivine [100] axes maximum. At greater depths, P waves propagation is the slowest parallel to the olivine [010] axes maximum.

The maximum S wave birefringence varies between 3.8 and 5.8 %.The fast split shear wave (S_1) is always polarized in a plane containing the propagation direction and the olivine [100] axes maximum. The maximum S wave polarization anisotropy is observed for waves propagating along the structural direction Y at all depths. The apparent isotropy direction, however, changes slightly with depth. It is always contained in the XZ plane (that is the plane that contains the lineation and the normal to the foliation), but it is very close to the lineation above 100 km depth, where axial-[100] olivine CPO patterns dominate, and at 45° to the lineation in the deeper layers, where the olivine CPO has an orthorhombic pattern.

The propagation of S_1 waves is always fastest along the foliation plane and slowest at high angle to it, close to the Z structural axis.However, the fastest propagation direction

SED
5, 963–1005, 2013

varies with depth. Between 70 and 90 km, it is parallel to the lineation and Y structural axis, while between 90–130 km, it is located at 45° to the lineation. At greater depths, S_1 waves propagation is fast in all directions within the foliation plane. In contrast, the S_2 waves propagation anisotropy does not change with depth. The fastest propagation direction of S_2 waves is always located on the XZ plane, at about 30° to the lineation, while the slowest velocities are found along the YZ plane. Finally, the V_p/V_{s_1} ratio is always maximum parallel to the alignment of olivine [100] axes and minimum along the YZ plane.

5 Discussion

5.1 Compositional effects on isotropic seismic properties

In the studied dataset, P and S wave velocities, V_p/V_s, and density vary with sample composition (Fig. 4). Melt depletion tends to decrease the density and V_p/V_s ratio, but to increase V_p and V_s. Metasomatism may result in refertilisation, that is, enrichment in pyroxenes and/or garnet, depending on the melt composition and depth. Enrichment in orthopyroxene decreases the whole rock density and P wave velocities, but increases S wave velocities and, hence, strongly reduces the V_p/V_s ratio. Garnet enrichment tends to strongly increase density and slightly P wave velocities and the V_p/V_s ratio.However, it has little to no effect on S wave velocities. The V_p/V_s ratio is more sensitive to orthopyroxene content than to the olivine Mg# or garnet content. Low V_p/V_s ratios are usually related to high S wave velocities. High V_s ($\sim 4.7\,\mathrm{km\,s^{-1}}$) and low V_p/V_s ratios (1.65–1.70) observed above the flat slab in central Chile–Argentina were indeed interpreted by Wagner et al. (2008) as due to orthopyroxene enrichment. Yet, although extremely high orthopyroxene contents (> 30 %) are observed in the Kaapvaal mantle xenoliths, this orthopyroxene-enrichment can at most produce V_p/V_s ratios of 1.7. These results are consistent with V_p/V_s ratios in mantle xenoliths from subduc-

SED
5, 963–1005, 2013

tion environments, in which reactive percolation of Si-rich fluids produced enrichment of orthopyroxene at the expenses of olivine (Soustelle and Tommasi, 2010).

Among the studied Kaapvaal peridotites, compositional changes results in density variations by up to 3 %, while V_p, V_s and V_p/V_s ratio vary by up to 2.4 % (Fig. 4). These variation ranges are slightly higher than the ∼ 2 % density and the 1.0–1.4 % V_s changes that Griffin et al. (2009) estimated to result from an increase of fertility by comparing data from domains where the crust has been stable since ≥ 2.5 Ga (Archons) and domains formed or modified at < 1 Ga (Tectons). They are, however, in agreement with the 2–3 % seismic velocity change due compositional variations estimated by Schutt and Lesher (2010) for the Kaapvaal mantle.

The calculated *P* wave velocities of Kaapvaal xenoliths at equilibrium pressure and temperature vary strongly at all depths. Between 90 and 150 km, the variation of *P* wave velocity at a given depth is of ∼ 1.2 %, but it reaches up to 2.3 % when the sheared peridotites that were equilibrated at greater depths are considered (Fig. 5). Such lateral heterogeneity in *P* wave velocity may be explained by the compositional heterogeneity of the cratonic root, as discussed above. This interpretation is corroborated by the strong variability of density at all depths (Fig. 5d). A lower proportion of deep sheared peridotites and a stronger compositional heterogeneity within the presently studied xenolith suite may explain the discrepancy between our *P* wave data and James et al. (2004) (Fig. 5a).

S waves velocity decreases and V_p/V_s ratio increase linearly by 3 % with increasing depth, while the density increases by about 2 %. These results are in good agreement with those obtained by James et al. (2004) (Fig. 5b–d). The observed variations are the result of the conjugate effects of pressure, temperature, and composition. To discriminate between thermal and compositional effects on *P* and *S* waves velocity profiles, we calculated the seismic properties of a sample with a standard composition (between 40–70 km: 65 % olivine with Mg#90, 23 % orthopyroxene, 12 % clinopyroxene; between 70 and 200 km: 65 % olivine with Mg#90, 20 % orthopyroxene, 10 % clinopyroxene, 5 % garnet), for both the cratonic geotherm estimated by Baptiste et al. (2012) and a "nor-

SED
5, 963–1005, 2013

mal" 100 km-thick lithosphere (Fig. 5). At first order, the change from a normal "normal" 100 km-thick lithosphere to a cratonic geotherm increases V_p and V_s by up to 2.8 and 3.1 %, respectively. This variation is on the same order of the one resulting from compositional heterogeneity among the Kaapvaal xenoliths (Figs. 4 and 5). In a 100 km thick lithosphere, the faster increase in temperature relative to pressure, results in decrease P and S waves velocity with depth; this trend is changed at sublithospheric depths, where the pressure effect becomes dominant, leading to an increase in seismic velocities. Within the cratonic mantle lithosphere, the slower temperature increase with depth is largely compensated by the increase in pressure, leading to almost constant P waves velocities and a weak decrease of S waves velocity with depth. The introduction of garnet at 70 km depth results in a sharp increase in both P wave and S waves velocities for both geotherms. The stronger increase in P wave velocities corroborates the stronger effects of the compositional changes on the P wave velocities relative to S waves.

The marked variations in density and S wave velocity among the deepest xenoliths (Fig. 5), which are mainly sheared peridotites, further highlight the strong compositional control on the isotropic seismic velocities. They may be attributed to the variations in the garnet content and in olivine Mg# that characterize the sheared peridotites (Fig. 4) and that have been attributed to refertilization shortly preceding mylonitisation and extraction by the kimberlite (Smith and Boyd, 1987; Baptiste et al., 2012).

5.2 Comparison with seismological velocity profiles and tomographic models for the Kaapvaal mantle

Comparison of the velocity profiles in Fig. 5 with one-dimensional P wave velocity profiles for the Kaapvaal highlights that most P wave models show an increase of velocity with depth between 50 and 200 km depth, consistent with James et al. (2004) data, but which we do not observe (Fig. 5a). Between 90 and 180 km, most models show values within the range of variation of the studied xenoliths, except the SATZ model of Zhao et al. (1999) and the global model IASP91. DataX model by Larson et al. (2006)

SED
5, 963–1005, 2013

is the model that fits the best our data, while QPM model by Qiu et al. (1996) is the most coherent with James et al. (2004) xenolith data.The decrease of V_p associated with the deep sheared peridotites between 180 and 200 km in the James et al. (2004) data is not fitted by any model. This observation reinforces the idea that these sheared peridotites correspond to very local modifications of the lithosphere caused and oversampled by kimberlites.Between 70 and 90 km, *P* waves velocities estimated for our xenoliths are higher than those in most seismic models. However, these depths are not well constrained in the present study because of the small number of xenoliths analyzed (2).

The discrepancy between 1-D seismic profiles and xenoliths velocities is still more marked for *S* waves (Fig. 5b). Most models do not fit neither our, nor James et al. (2004) xenolith-based profiles, except for the DataX model of Larson et al. (2006) and, in a lesser extent, the model L&B06 of Li and Burke (2006). The QPM model of Qiu et al. (1996) and the model of Hansen et al. (2009) (H09) display a marked decrease of V_s at 110–120 km that is not observed in the xenoliths data. The latter implies that the cratonic root is at least 180 km thick.

P and *S* wave tomography studies reported lateral velocity perturbations of 0.5 % (James et al., 2001; Fouch et al., 2004a), while surface waves studies imaged velocity perturbations as high as 5–7 % within the Kaapvaal cratonic root (Ritsema and van Heijst, 2000; Priestley et al., 2006; Chevrot and Zhao, 2007; Fishwick, 2010). Priestley and Tilmann (2009) attributed the velocity variations within the Kaapvaal lithospheric mantle to thermal effects. On the contrary, Begg et al. (2009) highlighted that xenolith thermometry implies a very narrow geotherms range and suggested that lateral *S* wave velocity variations within the cratonic root are mainly due to compositional changes. Lower velocities ($\sim$ 0.5 % for V_p and $\sim$ 0.8 % for V_s) imaged below the Bushveld complex by body-waves tomographies (James et al., 2001; Fouch et al., 2004a) (Fig. 1) have commonly been attributed to fertile compositions or to a recent thermal perturbation (Fouch et al., 2004a).This anomaly is not detected by surface-wave tomographies, probably due to their poorer lateral resolution (Priestley and Tilmann, 2009). The de-

SED
5, 963–1005, 2013

gree of variation of isotropic P and S wave velocities observed in the present study is higher, in particular for P waves, than any velocity perturbation imaged by body-wave tomographies, but cannot explain the strong velocity anomalies inferred from surface waves data. It is noteworthy that the variations in the xenoliths P wave velocity at all depths are stronger than the S wave ones, what renders the explanation of the strong S wave gradients inferred from surface waves still more difficult.

Partial melting within the lithosphere is a highly improbable cause for these velocity perturbations because of the cold geotherm beneath the Kaapvaal craton. The possible role of water content changes on seismic wave velocity is more difficult to discuss. Jacobsen et al. (2008) demonstrated that the combined effects of 3 mol% Fe and 0.8 wt% H_2O reduce the olivine shear and bulk moduli. However, the effects of low water contents, similar to those measured in the Kaapval peridotites (≤ 150 wt. ppm H_2O, Baptiste et al., 2012; Peslier et al., 2010) on olivine elastic properties are still poorly constrained.

Finally, at a given depth, the calculated variation in seismic velocity is almost as strong within xenoliths derived from a single pipe or from closely-spaced localities as within the entire dataset. V_p and V_s varies by up to 1.1 % for xenoliths from Kimberley equilibrated between 110 and 130 km depth (Fig. 5). V_p and V_s variation ranges of 2.1 % are attained in Jagersfontein xenoliths equilibrated between 150 and 170 km depth. V_p and V_s variations among xenoliths from closely-spaced pipes (Jagersfontein, Kimberley and DeBeers, which are all within 100 km, Fig. 1) may reach up to 1.2 % and 1.3 % between 110 and 130 km depth. Such small-scale variations cannot, however, be imaged by seismic tomography, which probably underestimates the heterogeneity of the subcratonic lithospheric mantle.

5.3 Seismic anisotropy

The changes in olivine CPO symmetry of the Kaapvaal peridotite xenoliths result in slight variations of the seismic anisotropy patterns (Fig. 2). Analysis of the individual samples seismic anisotropy shows strong variations at all depths (Table 1), but average

SED
5, 963–1005, 2013

values for different depth ranges are rather homogeneous (Fig. 6). Maximum P and S waves average anisotropies (Fig. 6) are coherent with the values for Kaapvaal mantle xenoliths reported by Long and Christensen (2000), but higher than those calculated by Ben Ismaïl et al. (2001). They are also coherent with the anisotropies calculated from Siberian xenoliths reported by Bascou et al. (2011).

The polarization and propagation anisotropies calculated for the Kaapvaal xenoliths may also be compared to seismic anisotropy data obtained using both body and surface waves, which sample therefore the Kaapvaal mantle root in different directions and with variable vertical and lateral resolutions. For instance, SKS splitting measurements have no vertical, but good lateral resolution (~ 50 km at lithospheric depths), whereas analysis of surface wave data with different periods allows discriminating between the lithospheric and sub-lithospheric contributions to seismic anisotropy. SKS and Rayleigh waves azimuthal anisotropy studies shows coherent fast SKS polarization and fast Rayleigh propagation at 70–120 s periods, which sample the lower lithosphere, characterized by a NNE–SSW orientation within the western and central part of the craton and an E–W orientation in the northern part (Silver et al., 2001; Adam and Lebedev, 2012). This suggests that the deep mantle lithosphere beneath the Kaapvaal displays olivine CPO with consistent orientations at the length scales of tens to hundreds of km.

We can also use the availability of both SKS splitting and surface waves anisotropy data in the Kaapvaal craton to try to determine the orientation of the foliation in the lithospheric mantle beneath the Kaapvaal craton. The idea is that both SKS and surface waves sample the same mantle lithosphere, which has a unique 3-D seismic anisotropy pattern, but SKS only probes the S wave polarization anisotropy in the vertical direction, while Rayleigh and Love waves travel along horizontal paths, allowing therefore to probe the S waves polarization and azimuthal anisotropies in the horizontal plane. To do so, we have determined the anisotropy that would be measured by SKS, Rayleigh (S_V) and Love (S_H) waves for 5 end-member orientations of the foliation and lineation (Fig. 7). A delicate point in this analysis is to determine whether S_H or S_V is the fast

SED
5, 963–1005, 2013

propagating S_1 wave, but this distinction can be made by analyzing the S wave polarization anisotropy in the horizontal plane for each case. S_1 is always polarized in a plane containing the lineation.Hence, when the lineation is vertical, S_1 correspond to S_V (Case 3). When it is horizontal, S_1 correspond to S_H (Case 1, 2 and 5). For a 45° dipping lineation (Case 4), the fastest wave is polarized in the horizontal or the vertical plane depending on the propagation azimuth. By carefully analyzing the trace of the lineation on the horizontal plane, we found that the horizontal plane displays the greatest anisotropies, implying that when significant anisotropy can be measured S_1 is equal to S_H.

If the foliation is horizontal (Case 1), SKS waves and S_V waves will measure similar polarization and azimuthal anisotropies comprised between 1.5 and 4.5 % in the mantle lithosphere, while S_H waves will detect almost no azimuthal anisotropy (≤ 1 %) at all depths. Because S_H is faster than S_V, the surface waves polarization anisotropy (ε) is higher than 1 at all depths. If the foliation is vertical and the lineation horizontal (Case 2), SKS waves sample a highly anisotropic direction (3.5 to 5.5 %) at all depths. The S_V waves propagation (2–4 %) anisotropy is at all depths twice as strong as the S_H waves one (1–2 %). As in case 1, the surface waves polarization anisotropy ε is higher than 1 at all depths. If the foliation and the lineation are vertical (Case 3), ε is smaller than 1, indicating that S_V is always faster then S_H. SKS and S_V waves will measure low anisotropies, comprised between 1.0 and 2.5 %. The anisotropy measured by S_H waves should be even lower (< 0.5 %). A 45° dipping foliation and lineation (Case 4) should produce SKS anisotropies higher than 2 % and S_V waves azimuthal anisotropy lower than 1 % between 80 and 120 km. At greater depths, SKS-waves anisotropy will be lower than 1 %, while S_V waves azimuthal anisotropy will vary between 1 and 2 %. The S_H waves azimuthal anisotropy will always be comprised between 1.5 and 2 %. The surface waves polarization anisotropy will be strongly dependent on the propagation direction. Finally, if we consider a 45° dipping foliation and a horizontal lineation (Case 5), the SKS and S_V waves should measure polarization and azimuthal anisotropies varying between 1.5 and 5 %, while S_H waves will measure azimuthal anisotropies

SED
5, 963–1005, 2013

lower than 2 %. As in cases 1 and 2, the surface waves polarization anisotropy is higher than 1, indicating that S_H is faster than S_V at all depths.

These predictions can be compared to the anisotropy detected using SKS and surface waves. Beneath the Kaapvaal craton, SKS delay times are low. Vinnik et al. (1995) first measured SKS delay times comprised between 0.4 and 1.4 s. Silver et al. (2001) obtained similar SKS delay times, between 0.3 and 1.1 s, with an average value of 0.62 s. Low delay times (0.15 to 0.75 s) were also obtained in a denser network near Kimberley by Fouch et al. (2004b). If we consider a 150 km-thick homogeneous anisotropic mantle lithosphere, which is consistent with 190 km-thick lithosphere inferred from the geotherm of Baptiste et al. (2012), these delay times yield anisotropies comprised between 0.9 and 3.4 %, with an average of 1.9 %. Such low SKS anisotropies are only obtained for either a vertical or a 45° dipping foliation and lineation (Cases 3 and 4 in Fig. 7).

Surface wave data consistently points to S_H faster than S_V in the Kaapvaal lithospheric mantle (Freybourger et al., 2001; S. Lebedev, personal communication, 2013). This is consistent with receiver functions data, which imaged a 160 km thick anisotropic mantle keel with vertical slow axis ($V_{S_H} > V_{S_V}$) and decreasing anisotropy with depth due to a decrease in V_{S_H} while V_{S_V} remains constant (Wittlinger and Farra, 2007). These observations are not consistent with Case 3 (Fig. 7), since vertical lineations always results in $V_{S_H} < V_{S_V}$.Moreover, coherent fast SKS polarization directions like those measured by Silver et al. (2001) are not expected if the lineation is vertical (Case 3). They might however be produced by a 45° dipping foliation (Case 4). Surface waves azimuthal anisotropies generated for Case 4 range between 0.5 and 3 %, being consistent with the low azimuthal anisotropies inferred in both global and regional surface wave models (Ekström, 2011; Adam and Lebedev, 2012). Case 4 produces, however, a S_H azimuthal anisotropy that is stronger than the S_V one, which is not consistent with the stronger Rayleigh azimuthal anisotropy (~ 2 %) relative to the Love azimuthal anisotropy (~ 1 %) imaged beneath South Africa in the global surface-wave model of Ekström (2011) and in the recent regional anisotropic tomography model for the Kaap-

SED
5, 963–1005, 2013

vaal by Adam and Lebedev (2012). Such a relation is obtained in the cases where the lineation is horizontal (Cases 1, 2, and 5 in Fig. 7), but it is accompanied by too strong Rayleigh azimuthal and SKS polarization anisotropies. Low SKS birefringence may result from vertical variations of the seismic anisotropy. Indeed, beneath the western Kaapvaal (Kimberley block), the Rayleigh waves azimuthal anisotropy show a change of fast propagation directions from NS within the crust to EW within the mantle (Adam and Lebedev, 2012). The weak SKS birefringence in the Kaapvaal craton might thus indicate that the deformation in the crust and the mantle are decoupled.

We do not observe any systematic change of the composition with depth in our dataset that could be related to the seismic discontinuity imaged by receiver functions at ~150 km depth (Wittlinger and Farra, 2007; Savage and Silver, 2008). Most cases presented in Fig. 7 show a decrease in anisotropy at 140 km depth, but the variation is too weak to produce a strong impedance contrast. In addition, Peslier et al. (2010) and Baptiste et al. (2012) did measure a marked decrease in OH concentrations in olivine at depths greater than 160 km. Yet the resulting change in elastic properties is probably too weak to explain the receiver function signal. A change in the orientation of the foliation and lineation might also produce an impedance contrast, but Rayleigh waves azimuthal anisotropy does not show significant variation of the fast direction within the mantle lithosphere (Adam and Lebedev, 2012). The physical causes producing the observed conversions remain therefore enigmatic.

6 Conclusions

The strong compositional heterogeneity of the Kaapvaal peridotite xenoliths results in up to 3 % variation in density, while V_p, V_s and the V_p/V_s ratio vary by ~2.3 %. These variations are slightly higher than the velocity perturbations imaged by body-wave tomography, but cannot explain the strong velocity anomalies reported by surface wave studies. Melt depletion tends to increase V_p and V_s and to decrease the V_p/V_s ratio and density. Orthopyroxene enrichment decreases the density and V_p, but increases

SED
5, 963–1005, 2013

V_s, strongly reducing the V_p/V_s ratio. Enrichment in garnet tends to increase the density strongly and slightly V_p and the V_p/V_s ratio, but has little to no effect on V_s. The V_p/V_s ratio is more sensitive to the orthopyroxene content than to olivine Mg# and garnet content. The present data also highlights that compositional heterogeneity in the Kaapvaal mantle root occurs at a scale much smaller than the one that may be sampled by seismic tomography, since at a given depth, the calculated variation in seismic velocity within xenoliths derived from a single pipe or from closely-spaced localities is almost as strong as within the entire dataset. Seismic tomography thus probably strongly underestimates the heterogeneity of the subcratonic lithospheric mantle.

Vertical density and seismic velocity profiles calculated using the xenoliths' compositions and equilibrium conditions show that V_s decreases, whereas the V_p/V_s ratio and density increase with increasing depth. V_p does not show a clear trend; it is highly variable at all depths, probably reflecting a greater sensitivity to modal composition changes. Comparison of these xenolith-based seismic profiles with 1-D velocity profiles derived from seismological data in the Kaapvaal highlights clear discrepancies between seismological and xenolith-based data. For *P* waves, the DataX model by Larson et al. (2006) fits the best our data, while QPM model by Qiu et al. (1996) is the most coherent with James et al. (2004) data. For *S* waves, most models, except for the DataX model of Larson et al. (2006) and, in a lesser extent, the model L&B06 of Li and Burke (2006), do not fit neither our, nor James et al. (2004) data, which imply that the cratonic root is at least 180 km thick.No seismological velocity model fits the decrease of V_p indicated by deep sheared peridotites between 180 and 200 km, reinforcing the idea that they represent very local modifications of the lithosphere caused and oversampled by kimberlites.

Changes in olivine CPO symmetry of the Kaapvaal peridotite xenoliths result only in slight variation of the seismic anisotropy patterns. Seismic anisotropy increases with olivine *J* index and olivine content, but there is no simple relation with the olivine CPO symmetry (BA index). Maximum anisotropy values range between 2.5 and 10.2 % for *P* waves azimuthal anisotropy (AV_p) and between 2.7 and 8 % for *S* waves polariza-

SED
5, 963–1005, 2013

tion anisotropy (AV_s) in agreement with existing xenolith data. The maximum *P* waves anisotropy of each 20 km interval varies between 4.5 and 7.9 %, whereas *S* waves anisotropy is comprised between 3.7 and 5.8 %. Models considering end-member orientations of the foliation and lineation in the subcratonic mantle lithosphere show that the simplest model that might produce both the coherent fast directions over large domains, but low delay times imaged by SKS studies, and the low azimuthal surface-waves anisotropy with S_H faster than S_V in the subcratonic mantle lithosphere is the presence of 45° dipping foliations and lineations.Horizontal or vertical lineations both fail to explain the observed seismic anisotropy.

Acknowledgements. The authors thank A. Vauchez and D. Mainprice for helpful discussions.D. Mainprice provided the programs for calculating seismic properties. C. Nevado and D. Delmas are thanked for providing high-quality polishing of sections for EBSD measurements. The EBSD-SEM national facility in Montpellier is supported by the Institut National de Sciences de l'Univers (INSU) du Centre National de la Recherche Scientifique (CNRS), France and by the Conseil Régional Languedoc–Roussillon, France.

References

Abramson, E. H., Brown, J. M., Slutsky, L. J., and Zaug, J.: The elastic constants of San Carlos olivine to 17 GPa, J. Geophys. Res., 102, 12253–12263, 1997.

Adam, J. M.-C.and Lebedev, S.: Azimuthal anisotropy beneath southern Africa from very broad-band surface-wave dispersion measurements, Geophys. J. Int., 191, 155–174, 2012.

Adams, A. and Nyblade, A.: Shear wave velocity structure of the southern African upper mantle with implications for the uplift of southern Africa, Geophys. J. Int., 186, 808–824, 2011.

Allsopp, H. L., Bristow, J. W., and Skinner, E. M. W.: The Rb–Sr geochronology of the Colossus kimberlite pipe, Zimbabwe, Transactions of the Geological Society of South Africa, 88, 245–248, 1985.

Baptiste, V., Tommasi, A., and Demouchy, S.: Deformation and hydration of the lithospheric mantle beneath the Kaapvaal craton, South Africa, Lithos, 149, 31–50, 2012.

SED
5, 963–1005, 2013

Bascou, J., Doucet, L. S., Saumet, S., Ionov, D. A., Ashchepkov, I. V., and Golovin, A. V.: Seismic velocities, anisotropy and deformation in Siberian cratonic mantle: EBSD data on xenoliths from the Udachnaya kimberlite, Earth Planet. Sc. Lett., 304, 71–84, 2011.
Begg, G. C., Griffin, W. L., Natapov, L. M., O'Reilly, S. Y., Grand, S. P., O'Neill, C. J., Hronsky, J. M. A., Poudjom Djomani, Y., Swain, C. J., Deen, T., and Bowden, P.: The lithospheric architecture of Africa: seismic tomography, mantle petrology, and tectonic evolution, Geosphere, 5,23–50, 2009.
Bell, D. R., Rossman, G. R., Maldener, J., Endisch, D., and Rauch, F.: Hydroxide in olivine: a quantitative determination of the absolute amount and calibration of the IR spectrum, J. Geophys. Res., 108, B2, ECV8.1–ECV8.9, 2003.
Bell, D., Grégoire, M., Grove, T., Chatterjee, N., Carlson, R., and Buseck, P.: Silica and volatile-element metasomatism of Archean mantle: a xenolith-scale example from the Kaapvaal Craton, Contrib. Mineral. Petr., 150,251–267, 2005.
Ben Ismaïl, W., and Mainprice, D.: An olivine fabric database: an overview of upper mantle fabrics and seismic anisotropy, Tectonophysics, 296, 145–157, 1998.
Ben Ismaïl, W., Barruol, G., and Mainprice, D.: The Kaapvaal craton seismic anisotropy: petrophysical analyses of upper mantle kimberlite nodules, Geophys. Res. Lett., 28, 2497–2500, 2001.
Chai, M., Brown, J. M., and Slutsky, L. J.: The elastic constants of an aluminous orthopyroxene to 12.5 GPa, J. Geophys. Res., 102, 14779–14785, 1997a.
Chai, M., Brown, J. M., and Slutsky, L. J.: The elastic constants of pyrope-grossular-almandine garnets to 20 GPa, Geophys. Res. Lett., 24,523–526, 1997b.
Chevrot, S. and Zhao, L.: Multiscale finite-frequency Rayleigh wave tomography of the Kaapvaal craton, Geophys. J. Int., 169, 201–215, 2007.
Collins, M. D. and Brown, J. M.: Elasticity of an upper mantle clinopyroxene, Phys. Chem. Miner., 26, 7–13, 1998.
Ekström, G.: A global model of Love and Rayleigh surface wave dispersion and anisotropy, 25–250 s, Geophys. J. Int., 187, 1668–1686, 2011.
Fishwick, S.: Surface wave tomography: imaging of the lithosphere-asthenosphere boundary beneath central and southern Africa?, Lithos, 120, 63–73, 2010.
Fouch, M. J., James, D. E., VanDecar, J. C., and van der Lee, S.: Mantle seismic structure beneath the Kaapvaal and Zimbabwe Cratons, S. Afr. J. Geol., 107, 33–44, 2004a.

SED
5, 963–1005, 2013

Fouch, M. J., Silver, P. G., Bell, D. R., and Lee, J. N.: Small-scale variations in seismic anisotropy near Kimberley, South Africa, Geophys. J. Int., 157, 764–774, 2004b.
Freybourger, M., Gaherty, J. B., Jordan, T. H., and the Kaapvaal Seismic Group: Structure of the Kaapvaal craton from surface waves, Geophys. Res. Lett., 28, 2489–2492, 2001.
Green, H. W. and Gueguen, Y.: Origin of kimberlite pipes by diapiric upwelling in upper mantle, Nature, 249,617–620, 1974.
Grégoire, M., Bell, D. R., and Le Roex, A. P.: Garnet lherzolites from the Kaapvaal craton (South Africa): trace element evidence for a metasomatic history, J. Petrol., 44, 629–657, 2003.
Griffin, W. L., O'Reilly, S. Y., Natapov, L. M.,and Ryan, C. G.: The evolution of lithospheric mantle beneath the Kalahari craton and its margins, Lithos, 71, 215–241, 2003.
Griffin, W. L., O'Reilly, S. Y., Afonso, J. C., and Begg, G. C.: The composition and evolution of lithospheric mantle: a re-evaluation and its tectonic implications, J. Petrol., 50, 1185–1204, 2009.
Hansen, S. E., Nyblade, A. A., Julià, J., Dirks, P. H. G. M., and Durrheim, R. J.: Upper-mantle low-velocity zone structure beneath the Kaapvaal craton from *S*-wave receiver functions, Geophys. J. Int., 178, 1021–1027, 2009.
Hielscher, R. and Schaeben, H.: A novel pole figure inversion method: specification of the MTEX algorithm, J. Appl. Crystallogr., 41, 1024–1037, 2008.
Isaak, D., Graham, E. K., Bass, J. D., and Wang, H.: The elastic properties of single-crystal fayalite as determined by dynamical measurement techniques, Pure Appl. Geophys., 141, 393–414, 1993.
Jacobsen, S. D., Jiang, F., Mao, Z., Duffy, T. S., Smyth, J. R., Holl, C. M., and Frost, D. J.: Effects of hydration on the elastic properties of olivine, Geophys. Res. Lett., 35, L14303, doi:10.1029/2008GL034398, 2008.
James, D. E., Fouch, M. J., Vandecar, J. C., and Van der Lee, S.: Tectospheric structure beneath southern Africa: The Kaapvaal Project: formation and evolutions of cratons, Geophys. Res. Lett., 28, 2485–2488, 2001.
James, D. E., Boyd, F. R., Schutt, D., Bell, D. R., and Carlson, R. W.: Xenolith constraints on seismic velocities in the upper mantle beneath southern Africa, Geochem. Geophy. Geosy., 5, Q01002, doi:10.1029/2003GC000551, 2004.
Jordan, T. H.: Composition and development of continental tectosphere, Nature, 274, 5671, 544–548, 1978.

SED
5, 963–1005, 2013

Kramers, J. D.and Smith, C. B.: A feasibility study of U–Pb and Pb–Pb dating of kimberlites using groundmass mineral fractions and whole-rock samples, Chem. Geol., 41, 23–38, 1983.
Kumazawa, M. and Anderson, O. L.: Elastic moduli, pressure derivatives, and temperature derivatives of single-crystal olivine and single-crystal forsterite, J. Geophys. Res., 74, 5961–5972, 1969.
Larson, M. A., Snoke, J. A., and James, D. E.: *S*-wave velocity structure, mantle xenoliths and the upper mantle beneath the Kaapvaal craton, Geophys. J. Int., 167, 171–186, 2006.
Li, A. and Burke, K.: Upper mantle structure of southern Africa from Rayleigh wave tomography, J. Geophys. Res., 111, B10303, doi:10.1029/2006JB004321, 2006.
Long, C. and Christensen, N. I.: Seismic anisotropy of South African upper mantle xenoliths, Earth Planet. Sc. Lett., 179, 551–565, 2000.
Mainprice, D.: A FORTRAN program to calculate seismic anisotropy from the lattice preferred orientation of minerals, Computat. Geosci., 16, 385–393, 1990.
Mainprice, D. and Humbert, M.: Methods of calculating petrophysical properties from lattice preferred orientation data, Surv. Geophys., 15, 575–592, 1994.
Mainprice, D. and Silver, P. G.: Interpretation of SKS-waves using samples from the subcontinental lithosphere, Phys. Earth Planet. In., 78, 257–280, 1993.
Mainprice, D., Barruol, G., and Ben Ismaïl, W.: The seismic anisotropy of the Earth's mantle: from single crystal to polycrystal, in: AGU Geophysical Monograph, edited by: Karato, A. M. F. S., Libermann, R. C., Masters, G., and Stixrude, L., AGU, Washington, DC, 117, 237–264, 2000.
Mainprice, D., Hielscher, R., and Schaeben, H.: Calculating anisotropic physical properties from texture data using the MTEX open source package, in: Deformation Mechanisms, Rheology and Tectonics: Microstructures, Mechanics and Anisotropy, edited by: Prior, D. J., Rutter, E. H., and Tatham, D. J., Geological Society, Special Publications, London, 175–192, 2011.
Pearson, D. G., Carlson, R. W., Shirey, S. B., Boyd, F. R., and Nixon, P. H.: Stabilisation of Archaean lithospheric mantle: a Re–Os isotope study of peridotite xenoliths from the Kaapvaal craton, Earth Planet. Sc. Lett., 134, 341–357, 1995.
Peslier, A. H., Woodland, A. B., Bell, D. R., and Lazarov, M.: Olivine water contents in the continental lithosphere and the longevity of cratons, Nature, 467, 78–81, 2010.
Phillips, D., Machin, K. J., Kiviets, G. B., Fourie, L. F., Roberts, M. A., Skinner, E. M. W.: A petrographic and $^{40}Ar/^{39}Ar$ geochronological study of the Voorspoed kimberlite, South Africa:

SED
5, 963–1005, 2013

implications for the origin of group II kimberlite magmatism, special issue, S. Afr. J. Geol., 101, 299–306, 1998.
Priestley, K.: Velocity structure of the continental upper mantle: evidence from southern Africa, Lithos, 48, 45–56, 1999.
Priestley, K. and Tilmann, F.: Relationship between the upper mantle high velocity seismic lid and the continental lithosphere, Lithos, 109, 112–124, 2009.
Priestley, K., McKenzie, D., and Debayle, E.: The state of the upper mantle beneath southern Africa, Tectonophysics, 416, 101–112, 2006.
Ritsema, J. and van Heijst, H.: New seismic model of the upper mantle beneath Africa, Geology, 28, 63–66, 2000.
Qiu, X., Priestley, K., and McKenzie, D.: Average lithospheric structure of southern Africa, Geophys. J. Int., 127, 563–587, 1996.
Savage, B. and Silver, P. G.: Evidence for a compositional boundary within the lithospheric mantle beneath the Kalahari craton from *S* receiver functions, Earth Planet. Sc. Lett., 272, 600–609, 2008.
Schutt, D. L. and Lesher, C. E.: Compositional trends among Kaapvaal Craton garnet peridotite xenoliths and their effects on seismic velocity and density, Earth Planet. Sc. Lett., 300, 367–373, 2010.
Sebai, A., Stutzmann, E., Montagner, J.-P., Sicilia, D., and Beucler, E.: Anisotropic structure of the African upper mantle from Rayleigh and Love wave tomography, Phys. Earth Planet. In., 155, 48–62, 2006.
Silver, P. G., Gao, S. S., Liu, K. H., and the Kaapvaal Seismic Group: Mantle deformation beneath southern Africa, Geophys. Res. Lett., 28, 2493–2496, 2001.
Silver, P. G., Fouch, M. J., Gao, S. S., Schmitz, M., and the Kaapvaal Seismic Group: Seismic anisotropy, mantle fabric, and the magmatic evolution of Precambrian southern Africa, S. Afr. J. Geol., 107, 45–58, 2004.
Simon, R. E., Wright, C., Kgaswane, E. M., and Kwadiba, M. T. O.: The *P* wavespeed structure below and around the Kaapvaal craton to depths of 800 km, from traveltimes and waveforms of local and regional earthquakes and mining-induced tremors, Geophys. J. Int., 151, 132–145, 2002.
Smith, D. and Boyd, F. R.: Compositional heterogeneities in a high temperature lherzolite nodule and implications for mantle processes, in: Mantle Xenoliths, edited by: Nixon, P. H., John Wiley, Hoboken, NJ, 551–561, 1987.

SED
5, 963–1005, 2013

Soustelle, V. and Tommasi, A.: Seismic properties of the supra-subduction mantle: constraints from peridotite xenoliths from the Avacha volcano, southern Kamchatka, Geophys. Res. Lett., 37, L13307, 1–5, 2010.
Suzuki, I., Anderson, O. L., and Sumino, Y.: Elastic properties of a single-crystal forsterite Mg_2SiO_4, up to 1,200 K, Phys. Chem. Miner., 10, 38–46, 1983.
Tommasi, A., Mainprice, D., Canova, G., and Chastel, Y.: Viscoplastic self-consistent and equilibrium-based modeling of olivine lattice preferred orientations: Implications for the upper mantle seismic anisotropy, J. Geophys. Res., 105, 7893–7908, 2000.
Tommasi, A., Godard, M., Coromina, G., Dautria, J.-M., and Barsczus, H.: Seismic anisotropy and compositionally induced velocity anomalies in the lithosphere above mantle plumes: a petrological and microstructural study of mantle xenoliths from French Polynesia, Earth Planet. Sc. Lett., 227, 539–556, 2004.
Tommasi, A., Vauchez, A., and Ionov, D. A.: Deformation, static recrystallisation, and reactive melt transport in shallow subcontinental mantle xenoliths (Tol Cenozoic volcanic field, SE Siberia), Earth Planet. Sc. Lett., 272,65–77, 2008.
Vinnik, L., Green, R. W. E., and Nicolaysen, L. O.: Recent deformation of the deep continental root beneath southern Africa, Nature, 375, 50–52, 1995.
Vinnik, L., Kiselev, S., Weber, M., Oreshin, S., and Makeyeva, L.: Frozen and active seismic anisotropy beneath southern Africa, Geophys. Res. Lett., 39,1–6, 2012.
Wagner, L. S., Anderson, M. L., Jackson, J. M., Beck, S. L., and Zandt, G.: Seismic evidence for orthopyroxene enrichment in the continental lithosphere, Geology, 36, 935–938, 2008.
Wang, Y., Wen, L., and Weidner, D.: Upper mantle S_H- and P-velocity structures and compositional models beneath southern Africa, Earth Planet. Sc. Lett., 297, 596–608, 2008.
Wasch, L. J., van der Zwan, F. M., Nebel, O., Morel, M. L. A., Hellebrand, E. W. G., Pearson, D. G., and Davies, G. R.: An alternative model for silica enrichment in the Kaapvaal subcontinental lithospheric mantle, Geochim. Cosmochim. Ac., 73, 6894–6917, 2009.
Webb, S. L.: The elasticity of the upper mantle orthosilicates olivine and garnet to 3 GPa, Phys. Chem. Miner., 16, 684–692, 1989.
Wittlinger, G. and Farra, V.: Converted waves reveal a thick and layered tectosphere beneath the Kalahari super-craton, Earth Planet. Sc. Lett., 254, 404–415, 2007.
Zhao, M., Langston, C. A., Nyblade, A., and Owens, T. J.: Upper mantle velocity structure beneath southern Africa from modeling regional seismic data, J. Geophys. Res., 104, 4783–4794, 1999.

SED
5, 963–1005, 2013

Table 1. Olivine Mg#, modal contents, equilibrium conditions, calculated seismic properties and densities of the studied Kaapvaal peridotites.

Locality	Sample	Ol Mg#	Modal compositions (%)				Temperature	Pressure	Depth	Density	Vp[1]
		(%)	Ol	Opx	Cpx	Gt	(° C)	(GPa)	(km)	(g cm^{-3})	(km s^{-1})
KIMBERLEY	KBBF6a	90.8	74	13	4	9	926	3.8	121	3.3690	8.27
	KBBF6b	91.0	82	8	4	6	908	3.7	118	3.3683	8.26
	KBBF8	94.3	81	19	0	0	1029	–	138	3.3500	8.19
	KBBF9	89.8	67	16	9	8	1102	4.7	149	3.3623	8.28
	KBBF10	92.4	72	27	1	0	948	–	125	3.3398	8.19
	KBBF11	93.6	88	11	1	0	1159	5.9	187	3.3618	8.17
	KBBF14	93.0	83	16	1	0	996	–	133	3.3518	8.20
	KBBF15	92.6	65	31	0	4	1067	4.3	137	3.3442	8.21
	KBBF16	93.3	71	26	0	3	–	4.0	127	3.3476	8.21
	KBBF18	92.2	75	17	6	0	850	–	110	3.3451	8.22
	KBBF20	–	65	35	0	0	800	–	102	3.3320[3]	8.17[3]
	FRB1402	93.2	83	9	0	8	1023	4.6	146	3.3770	8.25
	FRB1404	93.5	59	36	1	4	987	4.4	140	3.3380	8.21
	FRB1422	93.5	65	31	0	4	994	4.4	140	3.3442	8.21
	FRB1423	91.8	68	18	4	10	851	3.8	121	3.3658	8.28
	FRB1447	93.4	73	23	1	3	968	4.2	133	3.3501	8.22
	FRB348	92.3	58	28	7	7	938	3.7	118	3.3478	8.27
JAGERSFONTE	KBJ6	90.7	84	9	3	4	1163	4.9	152	3.3673	8.22
	KBJ8	90.9	87	13	0	0	1219	–	168	3.3689	8.21
	KBJ14	91.3	70	5	12	13	1140	4.7	149	3.3822	8.36
	KBJ30	89.4	63	11	11	15	1282	5.8	184	3.3813	8.35
	KBJ33	89.3	68	8	6	18	1217	4.8	152	3.3925	8.35
	KBJ52	92.7	75	25	0	0	900	–	118	3.3425	8.18
	KBJ54	92.3	75	23	2	0	907	3.8	121	3.3431	8.19
	KBJ56	92.5	65	28	0	7	895	3.5	111	3.3524	8.24
	KBJ60	91.5	86	13	1	0	1190	5.2	165	3.3574	8.17
	KBJ62	92.6	64	36	0	0	759	3.1	98	3.3311	8.18
	KBJ63	91.3	82	10	3	5	1250	4.9	156	3.3689	8.23
	J34	92.0	59	29	5	7	656	2.4	76	3.3457	8.26
	J41	92.4	61	39	0	0	668	3.7	118	3.3283	8.17
	J47	90.7	85	6	8	1	1227	4.7	149	3.3615	8.22
	J57	92.4	79	18	3	0	765	3.1	98	3.3457	8.21
	J63	87.7	78	10	10	2	1176	5.2	165	3.3581	8.23
MONASTERY	ROM23	92.2	66	28	4	1	910	3.3	105	3.3373	8.21
	ROM69	92.2	76	20	3	1	784	2.6	83	3.3438	8.22
LENTSENG	PHN4274	93.1	62	33	2	3	1015	4.3	137	3.3387	8.21
MOTHAE	PHN1925	89.9	63	22	11	4	1306	4.6	137	3.3462	8.26
KAMFERSDAM	PHN5580	92.6	73	27	0	0	–	–	–	3.2814[4]	8.34[4]
DE BEERS	KBB2	93.3	66	33	0	1	917	4.0	127	3.3363	8.19
PREMIER	FRB1330	91.3	80	17	3	0	744	–	93	3.3455	8.21
	FRB1336	88.9	70	30	0	0	–	–	–	3.3052[4]	8.28[4]
	FRB1339	91.7	71	18	8	3	–	–	–	3.3118[4]	8.33[4]
	PHN5266	92.7	70	26	4	0	–	–	–	3.3109[4]	8.29[4]
	PHN5267	91.3	70	19	6	5	1464	6.5	171	3.3667	8.29
FINSCH	FRB1501	93.0	70	22	0	8	1030	4.6	149	3.3620	8.24
	FRB1512	92.0	68	22	0	10	1058	4.7	149	3.3657	8.26
	FRB1513	92.6	70	27	1	2	1037	5.2	165	3.3443	8.19

SED
5, 963–1005, 2013

Table 1. Continued.

Locality	Sample	Max AV_p (%)	V_s^2 (km s^{-1})	Max AV_s pol (%)	Max AV_{s_1} (%)	Max AV_{s_2} (%)
KIMBERLEY	KBBF6a	9.7	4.67	8.0	4.8	6.0
	KBBF6b	9.2	4.66	7.0	3.5	5.9
	KBBF8	10.0	4.64	7.4	6.1	2.6
	KBBF9	5.4	4.65	4.2	2.8	2.1
	KBBF10	7.9	4.65	6.0	3.5	4.9
	KBBF11	4.7	4.55	3.3	4.6	2.9
	KBBF14	5.4	4.64	5.4	3.6	2.8
	KBBF15	5.2	4.65	4.7	1.2	4.5
	KBBF16	4.0	4.66	4.1	2.2	3.0
	KBBF18	7.2	4.67	6.3	4.6	3.7
	KBBF20	7.8[3]	4.67[3]	6.4[3]	3.2[3]	5.7[3]
	FRB1402	4.2	4.64	3.4	3.2	0.5
	FRB1404	3.2	4.67	3.2	2.6	2.4
	FRB1422	5.1	4.66	4.1	3.7	2.0
	FRB1423	7.2	4.69	5.5	2.8	3.7
	FRB1447	3.4	4.66	3.2	1.1	2.6
	FRB348	5.6	4.70	4.3	2.4	2.9
JAGERSFONTE	KBJ6	6.0	4.61	4.8	3.7	1.8
	KBJ8	10.2	4.60	6.8	2.3	6.4
	KBJ14	5.7	4.69	4.1	2.0	3.3
	KBJ30	4.5	4.66	3.9	2.5	1.6
	KBJ33	7.6	4.68	5.3	1.9	4.5
	KBJ52	7.3	4.64	5.7	4.1	3.5
	KBJ54	8.2	4.65	7.5	5.9	4.4
	KBJ56	6.3	4.69	5.4	5.1	2.3
	KBJ60	7.5	4.58	6.3	4.3	2.9
	KBJ62	7.3	4.68	7.4	4.4	5.6
	KBJ63	7.5	4.61	7.7	3.9	4.4
	J34	9.8	4.75	6.8	1.8	6.1
	J41	4.0	4.66	4.9	4.5	2.0
	J47	7.1	4.61	5.7	4.6	1.6
	J57	8.6	4.67	6.0	3.4	4.7
	J63	4.5	4.59	3.3	2.2	1.6
MONASTERY	ROM23	5.0	4.69	4.9	3.1	3.0
	ROM69	2.5	4.70	3.1	2.3	2.5
LENTSENG	PHN4274	3.5	4.66	3.5	3.0	2.5
MOTHAE	PHN1925	3.4	4.67	2.7	0.8	2.5
KAMFERSDAM	PHN5580	5.5[4]	4.89[4]	5.2[4]	4.0[4]	3.6[4]
DE BEERS	KBB2	6.8	4.67	5.7	2.6	4.5
PREMIER	FRB1330	9.4	4.68	6.7	2.3	6.1
	FRB1336	7.1[4]	4.85[4]	6.2[4]	4.9[4]	2.2[4]
	FRB1339	5.1[4]	4.86[4]	4.8[4]	3.8[4]	1.9[4]
	PHN5266	8.5[4]	4.86[4]	6.7[4]	5.0[4]	3.9[4]
	PHN5267	6.9	4.66	4.8	2.5	4.4
FINSCH	FRB1501	5.5	4.65	4.6	3.3	2.1
	FRB1512	5.0	4.66	4.1	3.3	1.9
	FRB1513	4.9	4.62	5.6	4.8	2.3

Ol mg#, modal content and P,T data from Baptiste et al. (2012).

[1] Mean *P* wave velocity.

[2] Mean *S* wave velocity.

AV_p: V_p azimuthal anisotropy;AV_s: V_s azimuthal anisotropy;AV_{s_1}: Fast V_s azimuthal anisotropy;AV_{s_2}: Slow V_s azimuthal anisotropy;maximum values.

[3] Seismic properties were calculated by only taking into account the sample equilibrium pressure and temperature, since olivine mg# was unknown.

[4] Seismic properties were calculated by only taking into account the mean olivine mg# of the sample, since the equilibrium conditions were unknown.

SED
5, 963–1005, 2013

Table 2. Elastic constants in Mbars calculated using Voigt–Reuss–Hill averaging and the elastic constants of enstatite (Chai et al., 1997a), diopside (Collins and Brown, 1998), garnet (Chai et al., 1997b), and olivine elastic tensors recalculated to account for the actual olivine Mg# in each sample, based on the single-crystal elastic constant tensors for fayalite, forsterite, and olivine with Mg# of 90, 91 and 93 (Kumazawa and Anderson, 1969; Suzuki et al., 1983; Webb et al., 1989; Isaak et al., 1993; Abramson et al., 1997).

Locality	Sample	C11	C22	C33	C44	C55	C66	C12	C13	C14	C15	C16
KIMBERLEY	KBBF6a	2.1600	2.6174	2.2429	0.7689	0.6740	0.7329	0.8049	0.8439	0.0014	0.0056	0.0159
	KBBF6b	2.1614	2.5764	2.2501	0.7556	0.6664	0.7421	0.8135	0.8370	−0.0054	−0.0156	0.0171
	KBBF8	2.0052	2.3564	2.4182	0.7834	0.6926	0.6801	0.7947	0.7908	0.0040	0.0156	−0.0021
	KBBF9	2.1736	2.4113	2.3372	0.7573	0.7079	0.7222	0.8452	0.8475	0.0018	0.0148	0.0131
	KBBF10	2.1134	2.4711	2.2052	0.7482	0.6726	0.7237	0.7736	0.7940	−0.0017	−0.0021	0.0095
	KBBF11	2.1584	2.3682	2.2252	0.7137	0.6704	0.7026	0.8370	0.8492	0.0017	0.0022	0.0063
	KBBF14	2.1386	2.3764	2.6650	0.7599	0.6847	0.7116	0.8074	0.8050	0.0022	0.0039	0.0031
	KBBF15	2.1818	2.3652	2.2124	0.7426	0.6903	0.7403	0.8056	0.8075	−0.0132	0.0132	0.0107
	KBBF16	2.2368	2.3379	2.1751	0.7433	0.7055	0.7431	0.8045	0.8074	0.0069	−0.0122	−0.0190
	KBBF18	2.1390	2.4690	2.2471	0.7535	0.6870	0.7203	0.7915	0.7984	0.0016	0.0000	−0.0016
	KBBF20	2.1224[1]	2.345[1]	2.1857[1]	0.7783[1]	0.705[1]	0.7222[1]	0.7523[1]	0.7805[1]	−0.0149[1]	−0.0033[1]	0.0159[1]
	FRB1402	2.2061	2.3580	2.3435	0.7481	0.7164	0.7143	0.8438	0.8511	0.0006	−0.0300	0.0054
	FRB1404	2.1869	2.3028	2.2378	0.7427	0.7145	0.7375	0.8114	0.7987	−0.0035	0.0001	−0.0175
	FRB1422	2.3020	2.1990	2.2797	0.7157	0.7279	0.7266	0.8119	0.7965	0.0052	0.0247	0.0476
	FRB1423	2.1669	2.4982	2.3049	0.7677	0.6995	0.7445	0.8137	0.8346	−0.0053	−0.0015	0.0073
	FRB1447	2.2415	2.3276	2.2290	0.7341	0.7024	0.7401	0.8055	0.8075	0.0019	0.0189	0.0064
	FRB348	2.3286	2.3646	2.1892	0.7347	0.7297	0.7578	0.8134	0.8002	−0.0027	0.0033	0.0421
JAGERSFONTEIN	KBJ6	2.2117	2.3819	2.3190	0.7547	0.6901	0.7053	0.8441	0.8364	−0.0029	−0.0033	0.0068
	KBJ8	2.1437	2.5764	2.1707	0.7389	0.6493	0.7355	0.8320	0.8593	0.0008	−0.0163	0.0267
	KBJ14	2.2506	2.4998	2.3425	0.7652	0.7101	0.7546	0.8722	0.8754	−0.0026	−0.0147	0.0115
	KBJ30	2.2488	2.4582	2.3794	0.7645	0.7093	0.7313	0.8902	0.8869	−0.0035	−0.0073	0.0065
	KBJ33	2.2248	2.5585	2.3411	0.7687	0.6996	0.7582	0.8629	0.8864	−0.0043	−0.0155	0.0232
	KBJ52	2.2035	2.4416	2.1234	0.7254	0.6871	0.7387	0.7953	0.7927	−0.0010	−0.0212	0.0079
	KBJ54	2.2153	2.2867	2.4037	0.7625	0.7020	0.6838	0.7860	0.7916	0.0009	−0.0192	−0.0310
	KBJ56	2.1418	2.3781	2.3544	0.7536	0.7152	0.7349	0.7922	0.8008	−0.0049	−0.0040	−0.0275
	KBJ60	2.0658	2.3988	2.2948	0.7523	0.6646	0.6907	0.8171	0.8336	0.0013	0.0039	0.0088
	KBJ62	2.1179	2.4316	2.1733	0.7726	0.6807	0.7351	0.7584	0.7640	−0.0004	0.0002	0.0022
	KBJ63	2.1334	2.4778	2.2230	0.7773	0.6667	0.7192	0.8461	0.8455	0.0009	−0.0028	−0.0023
	J34	2.1540	2.5660	2.1857	0.7884	0.6897	0.7790	0.7848	0.7536	−0.0031	0.0206	−0.0073
	J41	2.1366	2.2972	2.2589	0.7585	0.7003	0.7067	0.7728	0.7694	−0.0009	0.0057	0.0082
	J47	2.0888	2.4032	2.3554	0.7546	0.6832	0.6981	0.8293	0.8381	0.0013	0.0078	0.0090
	J57	2.2094	2.4552	2.1555	0.7644	0.6801	0.7316	0.7790	0.7931	−0.0047	0.0242	−0.0098
	J63	2.1674	2.3572	2.2985	0.7324	0.6919	0.7018	0.8557	0.8508	0.0028	0.0077	0.0073
MONASTERY	ROM23	2.1676	2.3192	2.2399	0.7534	0.7260	0.7418	0.7872	0.7800	0.0017	−0.0391	0.0188
	ROM69	2.2753	2.2929	2.2192	0.7600	0.7223	0.7367	0.7644	0.7835	−0.0031	−0.0066	0.0048
LENTSENG	PHN4274	2.1888	2.3263	2.2424	0.7428	0.7190	0.7144	0.7991	0.8029	0.0159	−0.0095	0.0013
MOTHAE	PHN1925	2.2229	2.3552	2.2732	0.7414	0.7096	0.7357	0.8226	0.8247	0.0003	−0.0066	−0.0004
KAMFERSDAM	PHN5580	2.1736[2]	2.373[2]	2.2914[2]	0.8095[2]	0.7614[2]	0.7901[2]	0.7172[2]	0.7128[2]	−0.0114[2]	−0.0046[2]	−0.0152[2]
DE BEERS	KBB2	2.1587	2.4200	2.1824	0.7440	0.6834	0.7392	0.7736	0.7905	−0.0042	0.0159	−0.0089
PREMIER	FRB1330	2.1317	2.5519	2.1425	0.7644	0.6702	0.7469	0.7729	0.7992	0.0000	0.0118	−0.0079
	FRB1336	2.2550[2]	2.1943[2]	2.3222[2]	0.8001[2]	0.7928[2]	0.7580[2]	0.7155[2]	0.7224[2]	0.0034[2]	0.5060[2]	−0.0450[2]
	FRB1339	2.2486[2]	2.3529[2]	2.3271[2]	0.7881[2]	0.7751[2]	0.7731[2]	0.7287[2]	0.7385[2]	−0.0001[2]	−0.0510[2]	0.0225[2]
	PHN5266	2.2466[2]	2.2858[2]	2.2703[2]	0.7922[2]	0.7830[2]	0.7936[2]	0.7158[2]	0.7234[2]	0.0008[2]	0.0552[2]	−0.0103[2]
	PHN5267	2.4937	2.2670	0.7534	0.6895	0.7366	0.8408	0.8572	−0.0078	−0.0324	−0.0068	0.8623
FINSCH	FRB1501	2.1482	2.4002	2.3306	0.7620	0.6975	0.7185	0.8152	0.8274	0.0056	0.0036	0.0002
	FRB1512	2.1689	2.3907	2.3505	0.7573	0.7040	0.7194	0.8214	0.8350	−0.0033	−0.0124	0.0012
	FRB1513	2.1300	2.3269	2.3105	0.7450	0.6878	0.6906	0.8008	0.8197	−0.0035	0.0182	0.0107

SED
5, 963–1005, 2013

Table 2. Continued.

Locality	Sample	C23	C24	C25	C26	C34	C35	C36	C45	C46	C56
KIMBERLEY	KBBF6a	0.8139	0.0077	0.0012	0.0161	0.0223	0.0120	0.0085	0.0093	−0.0051	0.0025
	KBBF6b	0.8165	−0.0169	−0.0058	0.0196	−0.0034	−0.0020	0.0029	0.0014	−0.0034	−0.0060
	KBBF8	0.8264	−0.0262	−0.0027	−0.0015	−0.0221	0.0196	−0.0003	0.0005	0.0002	−0.0073
	KBBF9	0.8649	0.0037	−0.0011	0.0113	0.0142	0.0134	−0.0016	0.0017	0.0014	0.0106
	KBBF10	0.7817	0.0137	−0.0029	0.0098	0.0062	−0.0029	−0.0009	0.0085	−0.0045	0.0041
	KBBF11	0.8611	0.0108	−0.0002	0.0021	0.0081	−0.0014	0.0031	0.0015	−0.0023	0.0055
	KBBF14	0.8123	0.0071	0.0015	0.0078	0.0184	0.0086	−0.0011	0.0014	0.0048	0.0007
	KBBF15	0.8058	0.0366	−0.0003	0.0216	0.0384	0.0086	−0.0018	0.0082	0.0064	0.0123
	KBBF16	0.8099	0.0041	0.0064	−0.0181	0.0121	−0.0032	−0.0052	−0.0141	−0.0067	0.0088
	KBBF18	0.7852	0.0088	−0.0005	0.0082	−0.0106	0.0001	−0.0001	0.0035	−0.0058	−0.0033
	KBBF20	0.8011[1]	0.0786[1]	0.0118[1]	−0.0034[1]	0.0558[1]	0.0001[1]	−0.0015[1]	−0.0004[1]	−0.0047[1]	0.0383[1]
	FRB1402	0.8454	−0.0018	−0.0036	0.0101	−0.0035	−0.0343	0.0014	0.0004	−0.0119	0.0008
	FRB1404	0.7990	−0.0050	−0.0008	−0.0227	0.0118	−0.0066	0.0046	−0.0170	−0.0052	0.0011
	FRB1422	0.7985	−0.0138	0.0052	0.0436	−0.0100	0.0027	−0.0066	0.0125	0.0113	0.0080
	FRB1423	0.8259	−0.0154	0.0053	0.0070	−0.0169	−0.0026	0.0002	0.0074	−0.0062	−0.0077
	FRB1447	0.8056	0.0197	0.0034	0.0024	0.0206	0.0117	−0.0047	0.0013	0.0030	0.0096
	FRB348	0.8119	0.0291	−0.0083	0.0346	0.0268	−0.0062	0.0003	0.1120	0.0065	0.0195
JAGERSFONTEIN	KBJ6	0.8614	−0.0092	−0.0002	0.0057	−0.0190	−0.0063	0.0057	−0.0046	0.0026	−0.0081
	KBJ8	0.8386	0.0163	−0.0106	0.0458	0.0111	−0.0170	−0.0025	0.0134	0.0023	0.0063
	KBJ14	0.8805	0.0071	−0.0025	0.0252	0.0048	−0.0145	−0.0014	0.0097	−0.0041	0.0023
	KBJ30	0.8980	0.0015	−0.0043	0.0035	−0.0037	−0.0091	0.0021	0.0019	−0.0036	−0.0019
	KBJ33	0.8917	0.0233	−0.0077	0.0316	0.0130	−0.0179	−0.0010	0.0107	−0.0034	0.0097
	KBJ52	0.7794	0.0118	−0.0097	−0.0143	0.0006	−0.0161	0.0058	0.0000	−0.0208	0.0015
	KBJ54	0.7927	0.0102	−0.0075	−0.0489	0.0442	−0.0174	−0.0112	−0.0221	−0.0137	0.0137
	KBJ56	0.7929	−0.0061	0.0041	−0.0509	0.0057	−0.0090	0.0138	−0.0006	0.0017	−0.0021
	KBJ60	0.8512	0.0038	−0.0005	0.0078	−0.0018	−0.0015	−0.0005	−0.0036	−0.0016	0.0030
	KBJ62	0.7763	−0.0364	−0.0035	−0.0210	−0.0027	−0.0119	0.0242	0.0064	−0.0182	0.0064
	KBJ63	0.8786	0.0027	−0.0027	−0.0058	−0.0035	0.0008	−0.0006	−0.0039	0.0019	−0.0003
	J34	0.7843	0.0087	0.0102	−0.0165	−0.0015	0.0214	0.0155	−0.0027	0.0061	0.0042
	J41	0.7780	0.0153	−0.0045	0.0012	−0.0179	−0.0023	−0.0053	−0.0083	−0.0013	0.0013
	J47	0.8698	−0.0066	0.0050	0.0071	0.0151	0.0097	0.0070	0.0045	0.0044	0.0033
	J57	0.7893	0.0281	0.0081	−0.0044	0.0180	0.0210	0.0053	−0.0027	0.0096	−0.0009
	J63	0.8719	−0.0123	0.0001	0.0047	−0.0180	0.0069	−0.0007	0.0001	0.0048	−0.0088
MONASTERY	ROM23	0.7975	−0.0075	−0.0016	0.0030	−0.0303	−0.0236	−0.0004	0.0099	−0.0185	−0.0103
ROM69	2.2753	0.7937	0.0035	−0.0124	0.0077	−0.0113	−0.0215	0.0036	0.0067	−0.0027	0.0010
LENTSENG	PHN4274	0.8002	−0.0199	0.0046	−0.0078	−0.0126	−0.0111	−0.0047	−0.0093	0.0020	0.0018
MOTHAE	PHN1925	0.8326	0.0183	0.0002	−0.0083	0.0241	−0.0057	0.0025	−0.0035	−0.0045	0.0109
KAMFERSDAM	PHN5580	0.7163[2]	−0.032[2]	−0.0143[2]	−0.0482[2]	−0.0107[2]	0.0071[2]	0.0256[2]	0.0069[2]	−0.0025[2]	−0.0085[2]
DE BEERS	KBB2	0.7725	0.0078	0.0013	−0.0088	−0.0025	0.0332	0.0139	0.0029	0.0004	−0.0014
PREMIER	FRB1330	0.7807	−0.0113	0.0042	−0.0089	−0.0004	0.0096	−0.0014	−0.0038	0.0043	−0.0007
	FRB1336	0.7226[2]	0.0491[2]	−0.0018[2]	−0.0439[2]	0.5300[2]	0.0431[2]	−0.0083[2]	−0.0238[2]	0.0174[2]	0.0145[2]
	FRB1339	0.7201[2]	−0.0199[2]	0.0122[2]	0.0136[2]	0.0031[2]	−0.0546[2]	0.0074[2]	0.0074[2]	−0.021[2]	−0.0110[2]
	PHN5266	0.7152[2]	−0.0564[2]	0.0136[2]	−0.0104[2]	−0.0565[2]	0.0743[2]	−0.0190[2]	−0.0308[2]	0.0413[2]	−0.0435[2]
	PHN5267	0.0021	−0.0138	−0.0110	0.0076	0.0076	−0.0234	−0.0131	−0.0111	−0.0134	−0.0067
FINSCH	FRB1501	0.8403	0.0012	0.0025	−0.0028	−0.0076	0.0036	−0.0067	−0.0033	−0.0004	−0.0007
	FRB1512	0.8417	−0.0001	−0.0122	0.0050	0.0042	−0.0250	−0.0024	−0.0016	−0.0056	−0.0014
	FRB1513	0.8198	0.0117	0.0038	0.0029	−0.0214	0.0035	0.0083	0.0037	0.0005	−0.0044

[1] Seismic properties were calculated by only taking into account the sample equilibrium pressure and temperature, since olivine mg# was unknown.
[2] Seismic properties were calculated by only taking into account the mean olivine mg# of the sample, since the equilibrium conditions were unknown.

SED
5, 963–1005, 2013

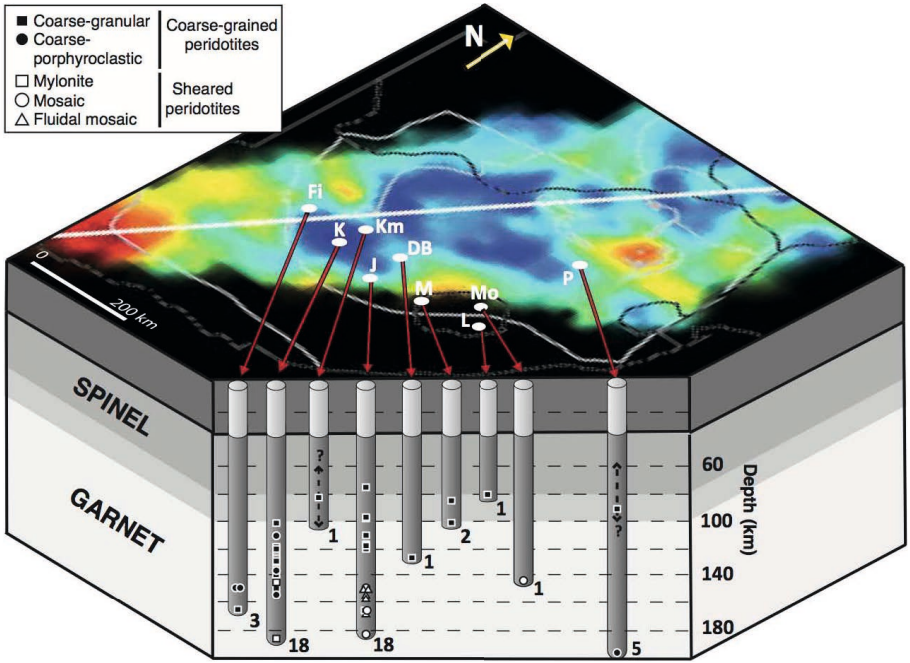

Fig. 1. Sketch displaying the location of the sampled kimberlitic pipes as well as the samples depth and microstructure (after Baptiste et al., 2012) relatively to the *S* waves tomography model of Fouch et al. (2004a) at 150 km. Fi: Finsch, K: Kimberley, Km: Kamfersdam, J: Jagersfontein, DB: De Beers, M: Monastery, Mo: Mothae, L: Lentseng, P: Premier.

SED
5, 963–1005, 2013

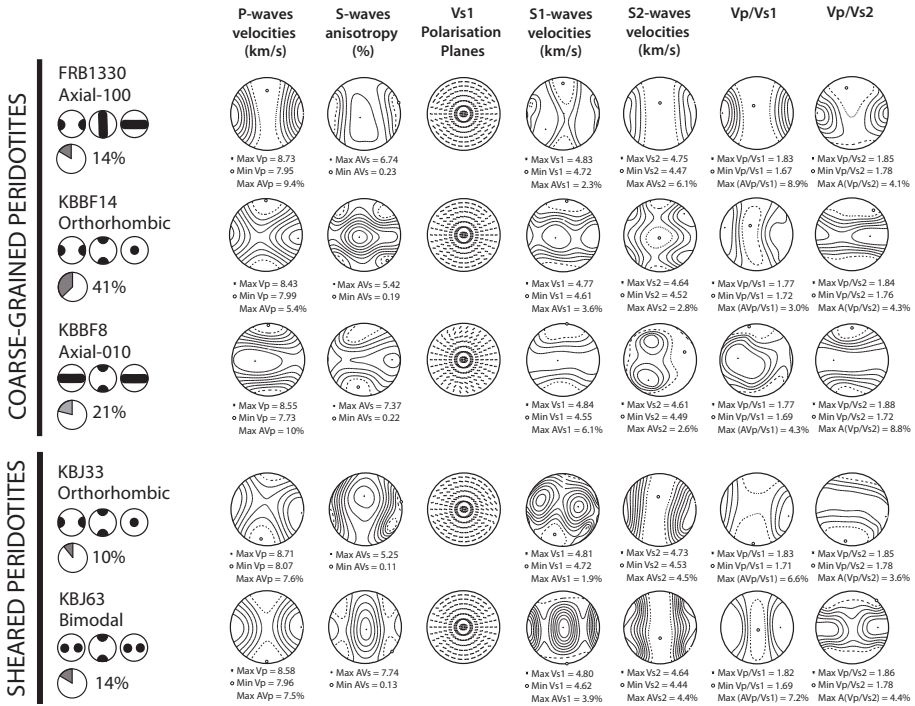

Fig. 2. Calculated seismic properties of Kaapvaal coarse-grained and sheared peridotites showing different olivine CPO patterns. From left to right, are displayed the 3-D distributions of: (1) *P* waves velocities (V_p), (2) *S* waves polarization anisotropy (V_s), (3) the orientation of fast shear wave polarization plane, (4) S_1 waves velocities (V_{S_1}), (5) S_2 waves velocities (V_{S_2}), (6) V_p/ V_{S_1} (7) V_p/V_{S_2}. Black squares and white spots indicate maximum and minimum values, respectively.

SED
5, 963–1005, 2013

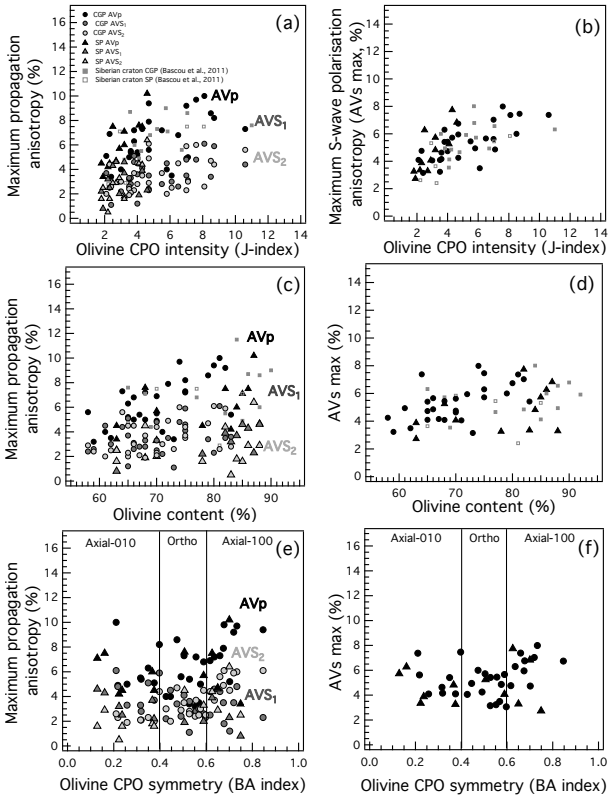

Fig. 3. Dependence of the maximum P, S_1 and S_2 waves anisotropy (AV_p, AV_{S_1} and AV_{S_2}), and of the maximum S waves polarisation anisotropy (AV_s) on the olivine CPO symmetry (characterized by the J index), the olivine content and the BA index.

SED
5, 963–1005, 2013

Seismic properties of the Kaapvaal craton mantle root

V. Baptiste and A. Tommasi

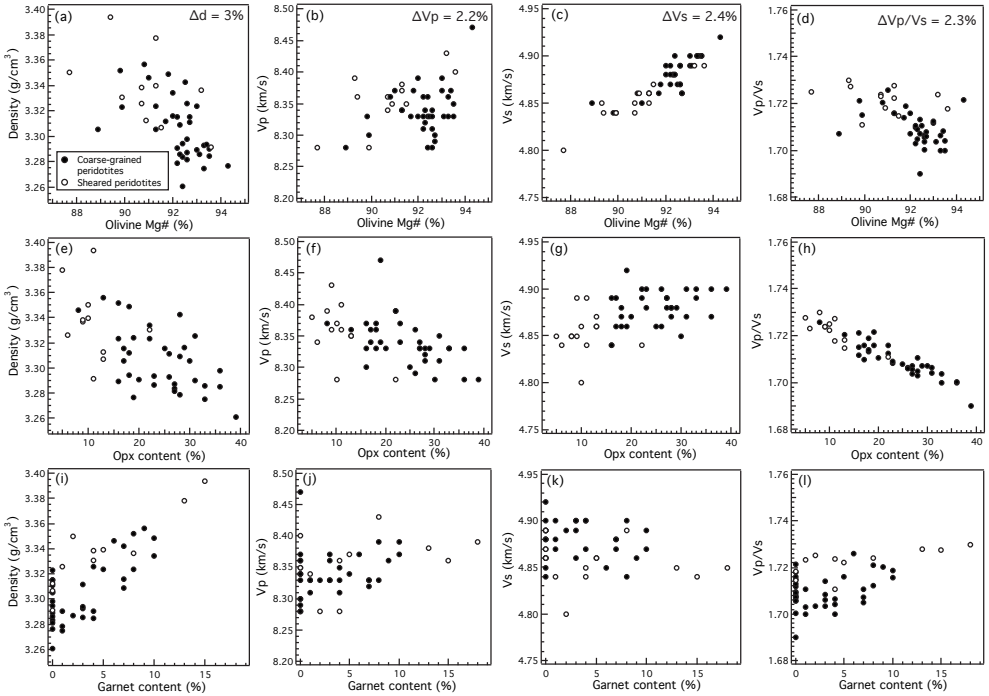

Fig. 4. Evolution of the samples density, *P* waves velocity (V_p), *S* waves velocity (V_s), and V_p/V_s ratio with olivine Mg#, orthopyroxene (opx) content, and garnet content.

SED
5, 963–1005, 2013

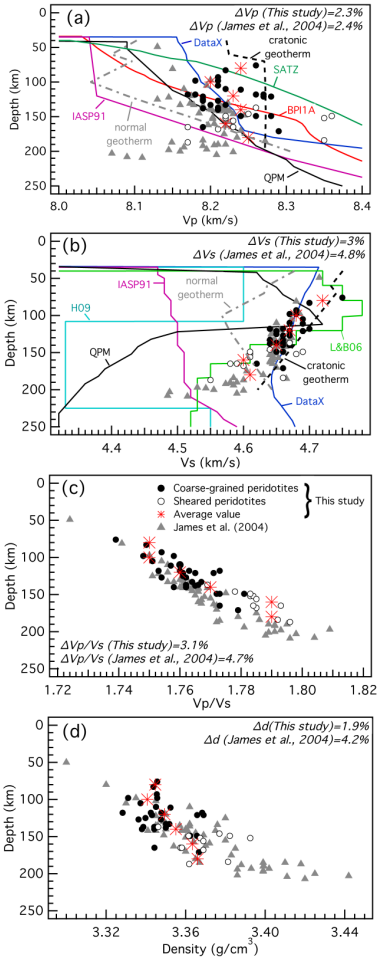

Fig. 5. Caption on next page.

SED
5, 963–1005, 2013

Seismic properties of the Kaapvaal craton mantle root

V. Baptiste and A. Tommasi

Fig. 5. Variation with depth the isotropic seismic velocities and density of the studied peridotite xenoliths : **(a)** V_p, **(b)** V_s, **(c)** V_p/V_s ratio, and **(d)** density. For comparison, the seismic properties of a peridotite with a standard composition (between 40–70 km: 65 % olivine with Mg#90, 23 % orthopyroxene, 12 % clinopyroxene; between 70 and 200 km: 65 % olivine with Mg#90, 20 % orthopyroxene, 10 % clinopyroxene, 5 % garnet) for both a "cratonic geotherm" as estimated by Baptiste et al. (2012) and a "normal geotherm" producing a 100 km thick lithosphere are shown as black and gray dashed lines, respectively The IASP91 reference model and different seismic models for southern Africa (BPI1A: Simon et al., 2002; DataX: Larson et al., 2006; H06: Hansen et al., 2009; L&B06: Li and Burke, 2006; QPM: Qiu et al., 1996; SATZ: Zhao et al., 1999) are also shown (colored lines).

SED
5, 963–1005, 2013

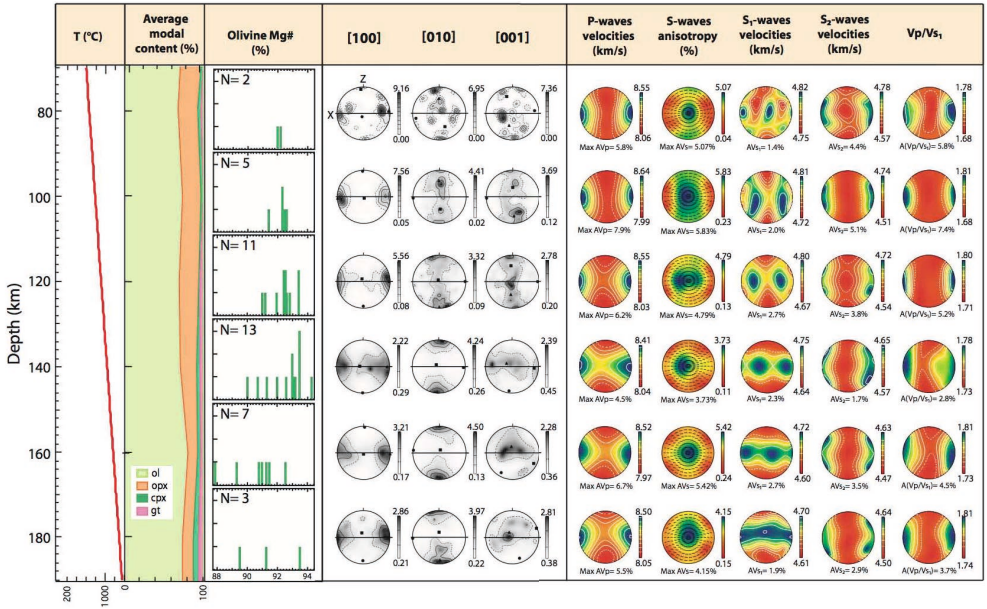

Fig. 6. Mean compositions, CPOs and seismic properties of five 20 km thick sections between 70 and 190 km depth calculated by averaging the olivine composition and modal contents of the samples originated from these depths. From left to right, are displayed: the geotherm of Baptiste et al. (2012), the average modal content of the samples, the number and the olivine Mg# of the samples in each depth section, the average olivine crystal-preferred orientations, and the 3-D distributions of *P* waves velocities (V_p), *S* waves polarization anisotropy (V_s), the orientation of fast shear wave polarization plane, S_1 waves velocities (V_{S_1}), S_2 waves velocities (V_{S_2}), and V_p/V_{S_1} ratios.

SED
5, 963–1005, 2013

Seismic properties of the Kaapvaal craton mantle root

V. Baptiste and A. Tommasi

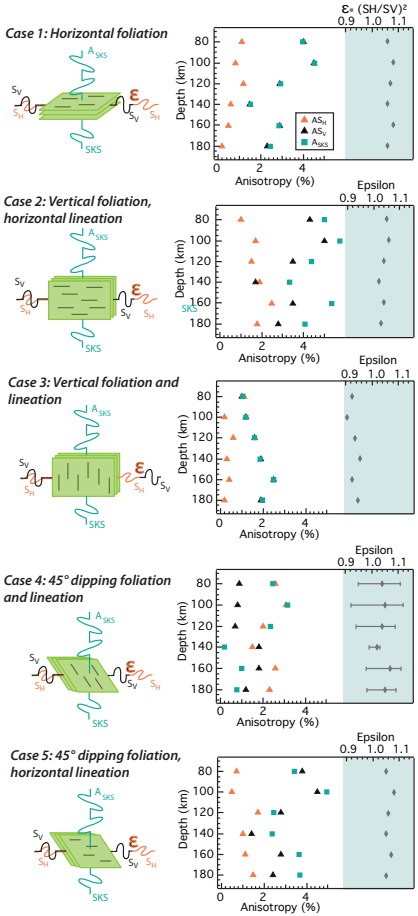

Fig. 7. Caption on next page.

SED
5, 963–1005, 2013

Fig. 7. Calculated surface waves polarization anisotropy ($\varepsilon = (S_H/S_V)^2$), maximum azimuthal anisotropy of horizontally propagating S_H and S_V, and the maximum SKS anisotropy for the depth-averaged samples in 5 different "end-member" orientations of the foliation and the lineation: (1) Horizontal foliation, (2) Vertical foliation with a horizontal lineation, (3) Vertical foliation and lineation, (4) 45° dipping foliation and lineation, and (5) 45° dipping foliation with a horizontal lineation.

SED
5, 963–1005, 2013